

1 **Title**

2 Paleotsunami record of the past 4300 years in the complex coastal lake system of
3 Lake Cucao, Chiloé Island, south central Chile

4

5 **Authors**

6 Philipp Kempf^{1,2}, Jasper Moernaut³, Maarten Van Daele², Mario Pino⁴, Roberto
7 Urrutia⁵, Marc De Batist²

8

9 **Affiliations**

- 10 1) Institute of Geological Sciences, Freie Universität Berlin, Berlin Germany
11 2) Renard Centre of Marine Geology, Ghent University, Gent, Belgium
12 3) Institute of Geology, University of Innsbruck, Innsbruck, Austria
13 4) Instituto de Ciencias de la Tierra, Universidad Austral de Chile, Valdivia, Chile
14 5) Centro EULA Chile, Universidad de Concepción, Concepción, Chile

15

16 **Abstract**

17 In CE 1960, Lake Cucao on Chiloé Island in south central Chile, was inundated by the
18 tsunami of the Great Chilean Earthquake (M_w 9.5). The area of what is now the lake
19 basin is submerged since the end of the rapid postglacial sea level rise and may have
20 recorded tsunami inundations in its sedimentary record since then. Sub-bottom
21 profiles and side scan sonar data reveal a tidal delta with a crosscutting channel,
22 which controls the sedimentary environment in the coast-facing part of Lake Cucao.
23 The convergent pattern of sub-bottom reflections near this channel indicates that tidal
24 currents were active in the lake at least episodically since the formation of a major
25 unconformity with strong reflection amplitude, i.e. the onset of lacustrine
26 sedimentation. A radiocarbon date at the base of one of the 21 collected sediment
27 cores dates this reflector to ~3800 yrs BP. Little net vertical displacement in
28 combination with an outlet river channel that can act as a pathway for sediment
29 transport appears to have maintained the sensitivity of Lake Cucao to record tsunamis
30 in its sedimentary record. The sub-bottom profiles show a succession of antidunes, of
31 which the geometry is used to reconstruct the flow speed and depth of the flow that
32 formed them to 6.8 m s^{-1} and 4.8 m, respectively. The sedimentary record contains 15
33 clastic layers which are interpreted as tsunami deposits with a varying level of
34 confidence. The confidence level on the tsunami interpretation depends on five
35 criteria; there are site-specific criteria, i.e. i) high magnetic susceptibility of the
36 sediment indicating high clastic content, ii) cross core correlation indicating
37 widespread deposition, iii) acoustic reflector correlation to the sedimentary record
38 (also indicating widespread deposition), and general criteria, e.g. iv) presence of mud
39 clasts, and v) age correlation to known paleotsunamis in the area. In this way 8 clastic

40 layers are interpreted as tsunami deposits with a high confidence level, 5 with a
41 medium confidence level and 2 with a relatively low confidence level. The
42 paleotsunami record of Lake Huelde, a mere 2 km north of Lake Cucao, contains 14
43 or 15 tsunami deposits in the same time interval, of which at least 10 can be
44 correlated. This study adds a long paleotsunami record on a coastline where extreme
45 tsunamis occur frequently and where long (>2000 yrs) paleotsunami records are still
46 sparse. This study underlines the many challenges and extraordinary advantages
47 associated to paleotsunami research on coastal lakes and demonstrates how
48 indispensable geophysical mapping and numerous coring sites can be in
49 understanding the depositional environment of dynamic coastal lakes for extracting
50 high-quality paleotsunami records.

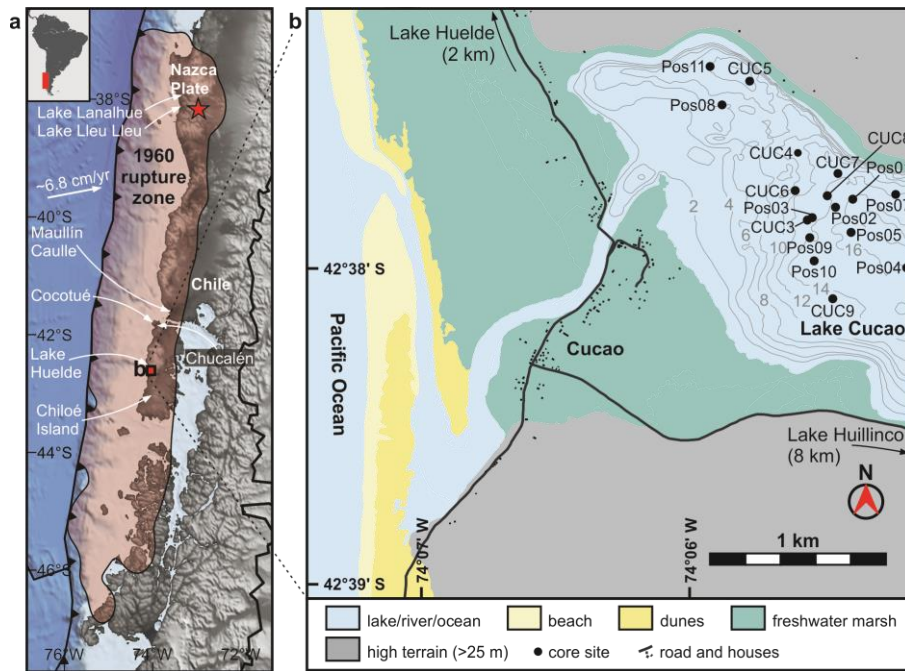
51 **Keywords**

52 Tsunami deposits, lacustrine sediments, sub-bottom profiles, south central Chile,
53 coastal sediment dynamics.

54 **1 Introduction**

55 Long and continuous sedimentary records of infrequent large-scale tsunamis are
56 essential in characterising recurrence patterns – a requisite for reliable hazard
57 assessments. During the past decades the scientific means to research the sedimentary
58 record of tsunamis have grown in quantity and quality (Chagué-Goff et al., 2017,
59 2011). Linking tsunami deposits to tsunamis from documented history is a necessary
60 step to calibrate tools in paleotsunami research. However, the primary reason for
61 sedimentological investigations is to extend the historical record which is often not
62 long enough to capture the variability in tsunami recurrence (Kempf et al., 2018). A
63 challenging task, because long and continuous sedimentary records in often highly
64 dynamic coastal areas are rare.

65 Written history in south central Chile begins with the Spanish invasion in CE 1541
66 (Cisternas et al., 2005; Lomnitz, 2004, 1970). In the ~500 years since then, four major
67 earthquakes were chronicled in the area between the Arauco peninsula (~37°S) and
68 the Chile Triple Junction (~46°S). The latest was the CE 1960 Great Chilean
69 Earthquake (M_w 9.5), notorious for being the strongest earthquake on instrumental
70 record. The older events occurred in CE 1575, 1737 and 1837. According to damage
71 reports, tsunamis damaged coastal towns in all but the CE 1737 earthquake.
72 Sedimentological investigations produced evidence for tsunami inundation for all
73 three documented tsunamis in a multitude of coastal areas of Chile (Atwater et al.,
74 2013; Cisternas et al., 2017, 2005; Dura et al., 2015; Ely et al., 2014; Garrett et al.,
75 2015; Kempf et al., 2015; Nentwig et al., 2015; Reinhardt et al., 2010). In addition,
76 six sites, i.e. Tirúa (Nentwig et al., 2018), Maullín (Cisternas et al., 2005), Caulle
77 (Atwater et al., 2013), Chucalén (Garrett et al., 2015), Cocotué (Cisternas et al., 2017)
78 and Lake Huelde (Kempf et al., 2017) are known to have recorded tsunami inundation
79 before written history began (Fig. 1). Of these six sites, only the Maullín and Lake
80 Huelde records extend the tsunami history past 1000 yrs BP, highlighting the need for
81 adequate sites that have recorded a long sedimentary tsunami record.

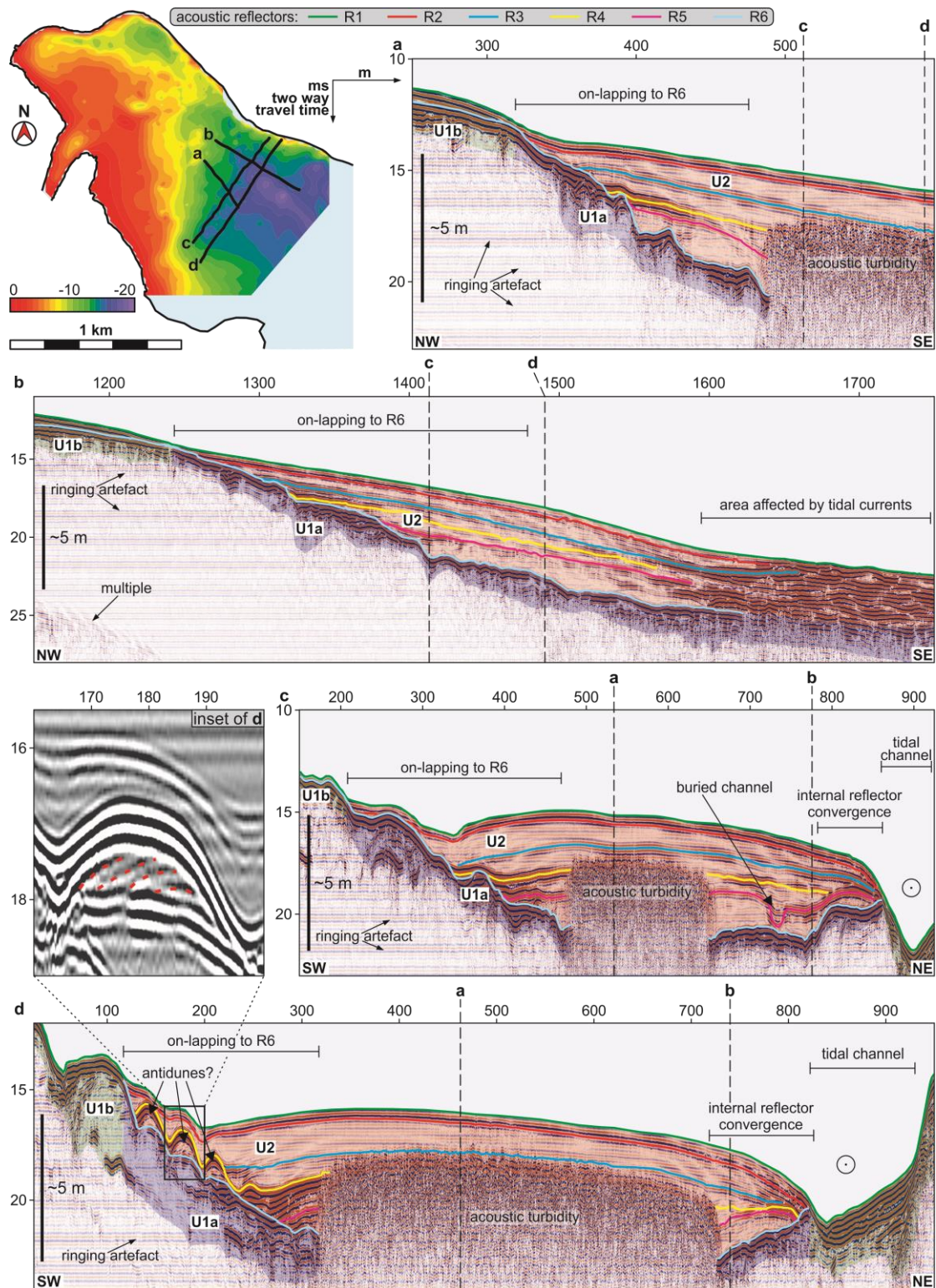


82

83 *Figure 1: a) Topographic and bathymetric overview of south central Chile. The*
 84 *digital elevation model is based on the ETOPO1 dataset (Amante and Eakins,*
 85 *2009). The epicentre and the 1 m slip contour line representing the rupture zone*
 86 *(Moreno et al., 2009) of the CE 1960 earthquake are drawn in red. Locations of*
 87 *coastal sediment records discussed in the text are indicated in white; b) detailed*
 88 *map of the study area. The geomorphological units are based on field*
 89 *observations and are extended using satellite imagery (Google Earth). The lake*
 90 *bathymetry map is based on side scan sonar bottom tracks (Kempf et al., 2015).*

91 One of the difficulties when researching tsunami deposits on millennial timescales, is
 92 relative sea level change, which plays a key role in tsunami deposition and
 93 preservation (Dura et al., 2016; Kelsey et al., 2015). Relative sea level rise creates the
 94 needed accommodation for tsunami deposit preservation in coastal lowlands.
 95 However, with too much relative sea level rise or fall or coastal erosion or
 96 progradation, the shoreline displacement may shift the area of tsunami deposition in
 97 respect to the previous tsunami deposit, which makes long and continuous
 98 paleotsunami records from coastal lowlands rare. In contrast, coastal lakes can
 99 provide excess accommodation and may be in a position with a stable sensitivity to
 100 record tsunami inundation since the culmination of the early Holocene sea level rise.

101 This study partially builds on a chapter in the doctoral thesis of the first author
 102 (Kempf, 2016). It presents a long and continuous sedimentary record from coastal
 103 Lake Cucao, with multiple tsunami deposits reaching back to ~4300 yrs BP based on
 104 a dense coverage of acoustic data and 21 sediment cores. The quality of the tsunami
 105 record is assessed by evaluating the sedimentary environment, tsunami deposit
 106 composition and age correlation with paleotsunamis in the region. The spatial
 107 multiproxy approach allows us to assign a confidence level to the interpretation as
 108 tsunami deposits, allowing a better evaluation of the temporal correlation of
 109 paleotsunamis.



110

111 *Figure 2: Sub-bottom profiles show the seismic stratigraphy of Lake Cucao with*
 112 *seismic units U1a (blue), U1b (green) and U2 (red). Profiles a) and b) parallel*
 113 *to the lake's long axis image the on-lapping of the internal acoustic reflectors*
 114 *R1–R5 onto acoustic reflector R6. Profiles in cross-direction to the lake's long*
 115 *axis c) and d) show down-lapping in the southeast and convergent internal*
 116 *reflectors towards the tidal channel. Reflector R4 expresses three hummocks (see*
 117 *inset), which are interpreted as antidunes.*

118 **2 Setting**

119 Lake Cucao (74.09°W, 42.63°S) is a coastal lake located on the west coast of Chiloé
120 Island in south central Chile (Fig. 1a). It is connected to the Pacific Ocean by its
121 outlet river channel, which crosses the 1.3 km wide barrier of an up to 250 m wide
122 beach, a narrow belt of active dunes followed by ancient dunes and pastures (Fig. 1b).
123 Lake Cucao is an elongated lake with its long axis in NW-SE direction of 7.9 km and
124 a width of ~1.5 km. It is 10.6 km² large and up to 25 m deep. It has a small catchment
125 to lake surface ratio of 3.1:1, because of the upstream adjacent Lake Huillinco. The
126 only direct riverine input is a small creek from the south in the eastern part. The outlet
127 channel of the lake facilitates water exchange between lake and ocean in both
128 directions, because the lake level lies in the intertidal zone (Kempf et al., 2015;
129 Villalobos et al., 2003). The daily exchange of water forms a stable saline bottom
130 water body in Lake Cucao and Lake Huillinco (Fig. 1) (Villalobos et al., 2003). With
131 the transport of water from the Pacific comes erosion, transport and deposition of
132 sediment, which produced a tidal delta around the outlet channel in Lake Cucao.
133 Active mega-ripples on the tidal delta and a crosscutting channel through the delta are
134 the bedform expressions of relatively strong present-day tidal currents (Fig. 2 and 3)
135 (Kempf et al., 2015).

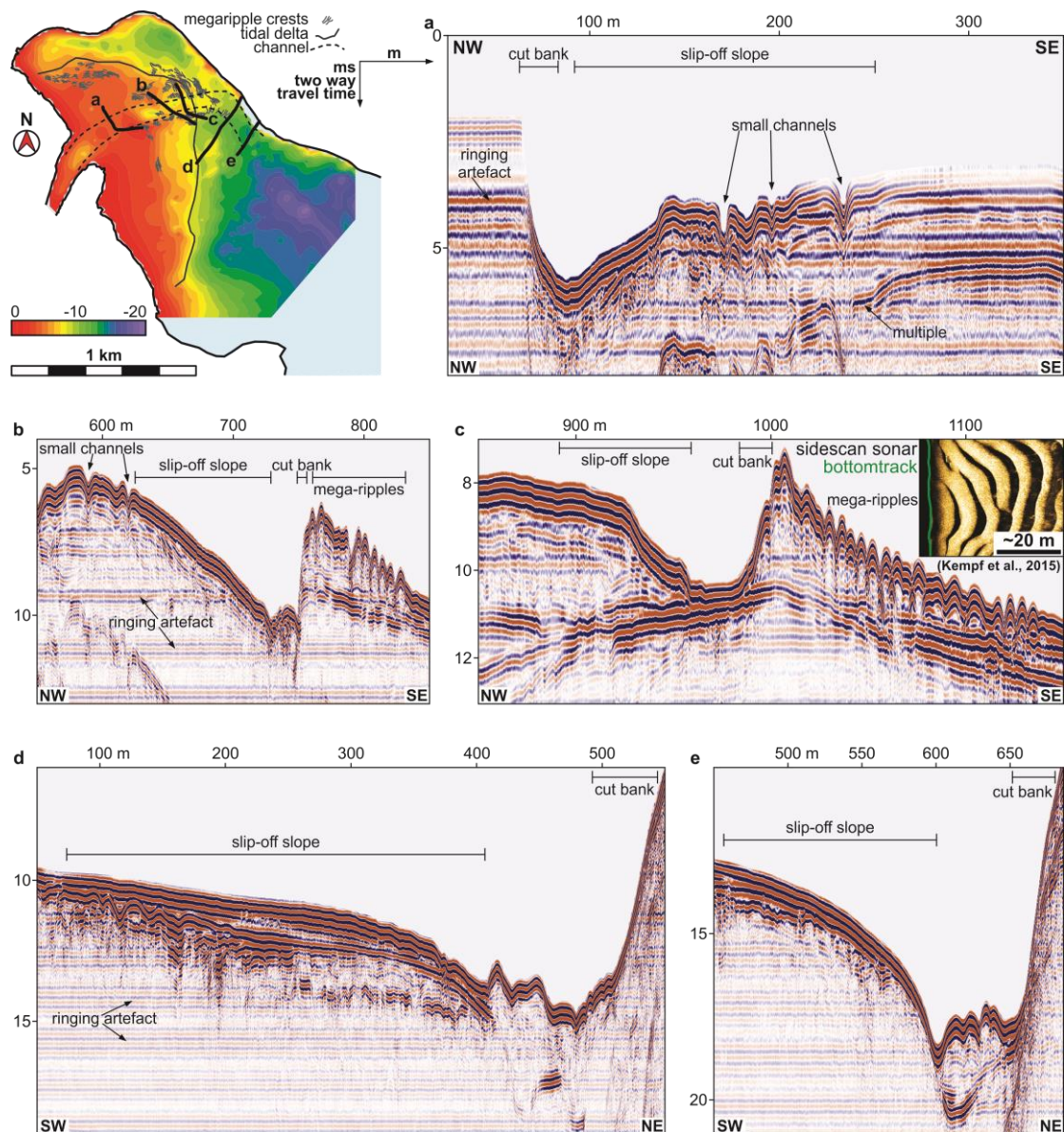
136 **3 Methods**

137 **3.1 Acoustic imaging**

138 The complex sedimentary system around Lake Cucao's outlet, was imaged with a
139 Klein3000 side scan sonar, which uses 100 kHz and 500 kHz frequencies to produce a
140 50 m wide swath of the lake floor's acoustic reflectivity. The data was visualised with
141 SonarWizMap v4 and has been presented in detail in Kempf et al. (2015). Here, we
142 make use of the mapped mega-ripple crest outlines (Fig. 3).

143 We collected 25 km of high-resolution sub-bottom profiles with a 3.5 kHz
144 GeoAcoustics GeoPulse pinger in 71 lines. At 3.5 kHz, the vertical resolution is
145 between 10 and 20 cm. The data was visualised and interpreted with IHS Markit
146 Kingdom v8.8. We use the sub-bottom profiles to

- 147 i) image the sedimentary architecture of the lake basin infill,
- 148 ii) to map geomorphologic features.
- 149 iii) to describe the general seismic stratigraphy,
- 150 iv) to determine coring sites,
- 151 v) to integrate the sediments cores with the acoustic data (ground truthing)



152

153 *Figure 3: Sub-bottom profiles across the tidal channel expressing the asymmetry of*
 154 *the channel with alternating slip-off slopes and cut banks. Tidal currents*
 155 *produce mega-ripples outside the cut bank and small channels are present on the*
 156 *upper bank of the slip-off slope.*

157 **3.1 Sediment core analysis**

158 In total, we cored at 21 locations in Lake Cucao, 9 of which were cored deeper than 2
 159 m burial depth, with a maximum of ~8 m burial depth recovered. The top core section
 160 at each coring site is comprised of a gravity core, because gravity corers produce
 161 relatively undisturbed near-surface sediment samples. Any deeper core sections were
 162 obtained with a UWITEC hammer-driven piston corer. Deep and full recovery was
 163 achieved by overlapping 3-m-long core sections to produce composite cores. Both
 164 types of cores have a 6 cm inner diameter.

165 Each split core was analysed with a multi-sensor core logger (Geotek MSCL) for
 166 high-resolution line scan core surface imagery, gamma ray attenuation density

167 logging and magnetic susceptibility logging (Bartington MS2E point sensor). The
 168 organic content was estimated using protocols in Heiri et al. (2001) for loss on
 169 ignition to 550 °C. Some core sections were X-ray CT-scanned with a Siemens Flash
 170 medical CT-scanner with a voxel size of $\sim 0.15 \times \sim 0.15 \times 0.6$ mm. Grain size
 171 distributions were measured with a Malvern Mastersizer 2000 after treatment with 2
 172 ml of 35% hydrogen peroxide to dissolve organic content (where necessary this step
 173 was repeated), 1 ml of 10% nitric acid to dissolve calcareous content and 300 mg
 174 sodium hexametaphosphate to prevent grain flocculation. Material for radiocarbon
 175 dating was extracted by either identifying macrofossils or by wet-sieving 1 cm thick
 176 slices of sediment and picking remains of plants and periostraca in the sieve (Tab. 1).

177 The age control is based on 7 radiocarbon dates (Tab. 1) and the results of Kempf et
 178 al. (2015), who identified the youngest clastic layer as the CE 1960 tsunami deposit
 179 by the means of ^{137}Cs and ^{210}Pb -dating. The radiocarbon dates were calibrated using
 180 the southern hemisphere calibration curve SHCal13 (Hogg et al., 2013). The samples
 181 are comprised of leaves, small plant fragments and periostraca of (probably) *Diplodon*
 182 *chilensis* and fragments thereof. *Diplodon chilensis* is a freshwater species
 183 (Valdovinos and Pedreros, 2007).

184 *Table 1: Radiocarbon data for fossil leaves, plant fragments and periostraca from*
 185 *composite core Pos04, which is used as the master core for the age-control of*
 186 *the Lake Cucao sedimentary record.*

sample ID	core ID	section depth	core depth in event-free age model	material	lab ID	14Cage	14Cage error
		cm	cm			14C yrs BP	yrs
CUCA10B-1.5	CUCA10B	1.5	142.5	shell fragment and plant fragments	UBA-37365	26178	161
CUCA10B-51	CUCA10B	51	190	plant fragments	UBA-37369	5189	56
CUCA11A-52	CUCA11A	52	246	plant fragments	UBA37370	2360	63
CUCA11A-101.5	CUCA11A	101.5	285.5	plant and periostracum fragments	UBA-37368	2166	34
CUCA11B-22	CUCA11B	22	313	plant fragments	UBA-37367	2342	33
CUCA11B-91.5	CUCA11B	91.5	353.5	periostracum	UBA-37364	2829	38
CUCA12B-82.5	CUCA12B	82.5	504	leaf	UBA-21476	3445	34

187

188 4 Results

189 4.1 Seismic stratigraphy

190 Two seismostratigraphic units can be differentiated on sub-bottom data from Lake
 191 Cucao, U1 and U2 (Kempf et al., 2015). U1 (a and b) includes the acoustic base of the
 192 sedimentary infill. They laterally merge into one another. U1a is covered by the lake's
 193 sedimentary infill in relatively deep areas, whereas U1b is at least sporadically
 194 reworked by tidal currents entering and exiting the lake in shallow areas near a tidal
 195 channel and not covered by lake infill (Fig. 2). U2 is the lacustrine sediment infill.
 196 The basal contact of U2 to U1a creates an unconformity (reflector R6) characterized
 197 by on-lapping reflector terminations towards the west. The internal reflector geometry
 198 of U2 in the upper part (above reflector R4) is parallel to sub-parallel with a low-
 199 amplitude acoustic facies including infrequent high amplitude, continuous reflections.

200 (Fig. 2c). The lower part of U2 (below reflector R4) describes a more complex infill
201 pattern with few internal unconformities.

202 The presence of shallow gas in the sediment of the central basin causes acoustic
203 turbidity, which blanks the internal reflector geometry of U2 at depths greater than
204 ~1.5 m (2 ms two-way-travel time, TWT). In total, five parallel to sub-parallel
205 reflectors (R1–R5) can be traced within U2. R1 represents the lake floor and produces
206 a continuous, strong reflection with decreasing amplitude towards the deeper lake
207 basin in the southeast (Fig. 2). R2–R5 show high-amplitude, continuous internal
208 reflections and form on-laps to either R6 or to one of the other internal reflectors, e.g.
209 R4 on-laps to R5 in some areas. Of all internal reflectors, R4 has the highest reflection
210 amplitude and marks the top of a hummocky paleo-surface in the south of the
211 surveyed area (Fig. 2d). The hummocks are ~30 m long and ~1 m thick with up-slope
212 dipping internal reflections. The two lowermost internal reflectors, R4 and R5, exhibit
213 erosion of the underlying acoustically transparent lake sediment in the form of few
214 buried channels (Fig. 2c).

215 The tidal channel incises the shallow delta up to 3.5 m deep and ~100 m wide, at its
216 western end as a prolongation of the outlet river channel (Fig. 3a). The bathymetric
217 cross-profiles of the channel are asymmetric with a flatter slip-off slope and a steeper
218 cut bank of the channel (Fig. 3). The asymmetry alters along the channel. About 10 m
219 wide and 0.5 m deep incised channels are common on the upper slip-off slope. Mega-
220 ripples with about 8 m ripple wavelength and ~0.4 m ripple height are abundant
221 around the incised channel, with a concentric arrangement (Kempf et al., 2015). The
222 channel continues towards the north-eastern shore (Fig. 3b, c) and bends south-
223 eastward to align with the long axis of the lake from where it continues parallel to the
224 north-eastern shoreline (Fig. 3d, e). Towards the channel, the parallel to sub-parallel
225 sedimentary infill of U2 (R1–R5) becomes convergent (Fig. 2c, d).

226 **4.2 Lacustrine sedimentation**

227 On the intertidal delta and in the crosscutting channel, i.e. areas where the top of U1b
228 is at the lake floor, the sediment consists of a well-sorted medium to fine sand with
229 mostly quartz, feldspar, hornblende and mica minerals (Fig. 4, e.g. core CUC7). The
230 coarse and moderately to well sorted sand prevented penetration deeper than 20 cm
231 with the coring equipment in these locations. This sand is mostly massive with some
232 occurrences of 1 cm thick grey muddy layers. The magnetic susceptibility of this sand
233 is very high, sometimes exceeding 1000×10^{-5} SI.

234 Sediment from the lake basin consists mostly of brown to black homogenous, poorly
235 sorted organic-rich mud. The transition from black to brown mud can be gradual or
236 sharp. In the case of sharp transitions, the brown mud is on top. The organic content
237 for both black and brown mud is between 20 and 35 % and consists of seeds, fibrous
238 plant material, pollen and fragments of bivalve periostraca without the calcareous
239 shell. The periostraca are sometimes fully preserved with distinct growth rings and are
240 probably from *Diplodon chilensis*, the most common freshwater clam in southern and

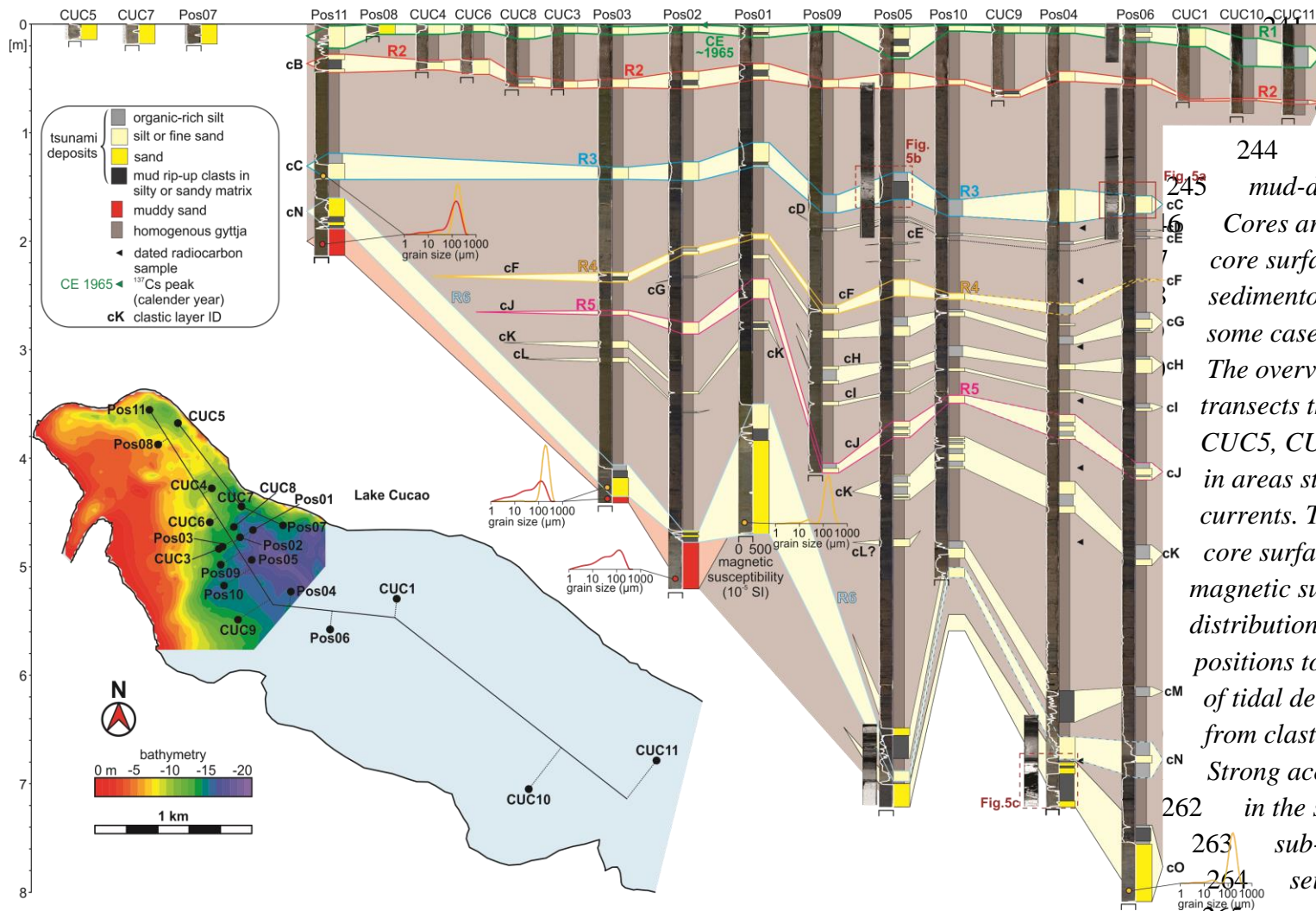
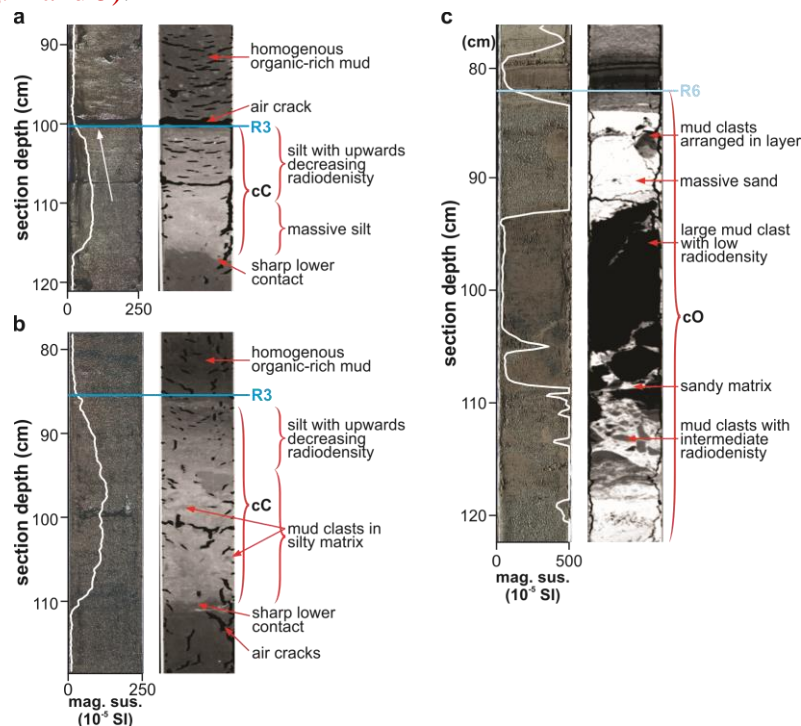


Figure 4: Core to core correlation of clastic 244 layers in the organic-rich mud-dominated lake sediments. Cores are represented by a split core surface image, a sedimentological core log and in some cases 2D slices of CT-scans. The overview map shows two core transects through the lake. Cores CUC5, CUC7 and Pos07 are located in areas strongly affected by tidal currents. The white line on the split core surface images represents magnetic susceptibility. Grain size distributions are shown in 7 different positions to differentiate muddy sand of tidal delta foresets (red lines) from clastic layers (orange lines). Strong acoustic reflectors are drawn in the same colour as they are on sub-bottom profiles. The seismic to core correlation is captured in figure 6.

266 south central Chile. The organic-rich mud smells strongly of hydrogen sulphide when
 267 cores are opened the first time (both during fieldwork and in the lab), indicating
 268 hypoxic or anoxic conditions. The magnetic susceptibility is low between 0 and 40 ×
 269 10⁻⁵ SI (Fig. 4 and 5).

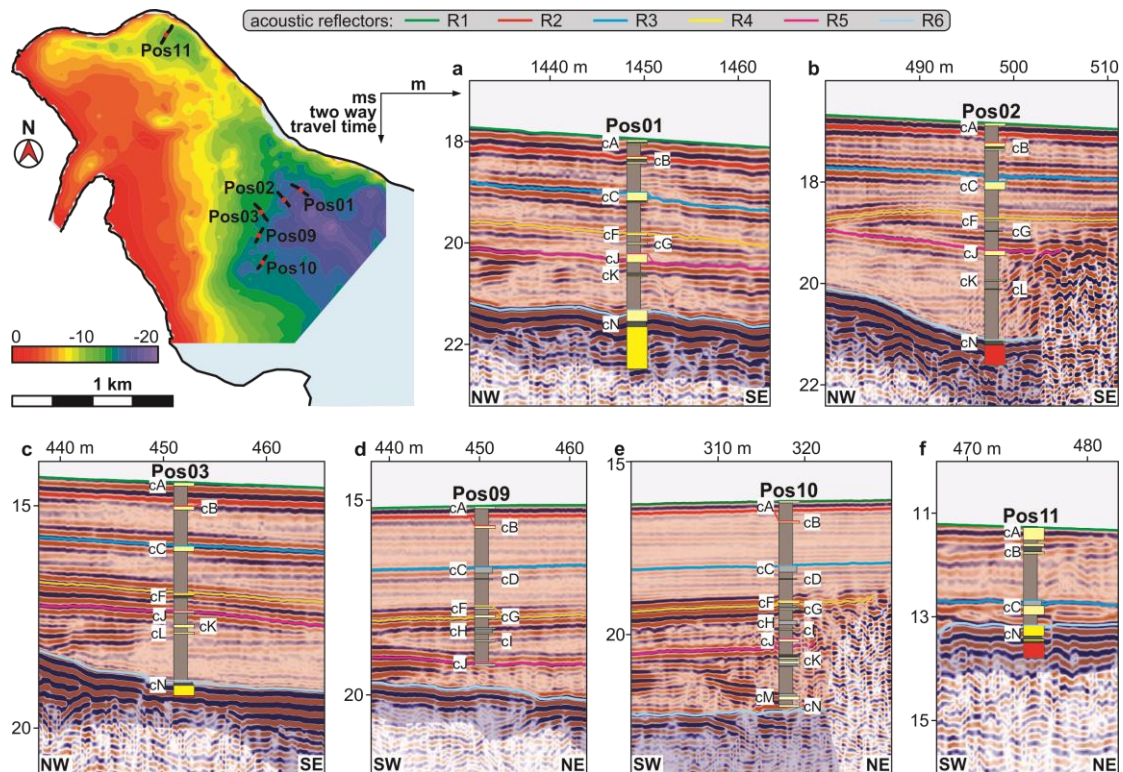


270
 271 *Figure 5: X-ray CT-scans of selected core sections. Lighter grey means higher*
 272 *radiodensity. a) and b) CT-scans of clastic layer cC associated acoustic reflector*
 273 *R3; c) clastic layer cN under acoustic reflector R6. All clastic layers exhibit a*
 274 *sharp contact at the bottom. CT-scans in a) and b) show upwards decreasing*
 275 *radiodensity. In b) and c) mud clasts with two differing CT-densities are*
 276 *surrounded by silty (b) to sandy (c) matrix.*

277 In all 9 long cores, there are 1 to 30 cm thick layers with high clastic content. The
 278 medium silt to fine sand of the clastic layers is coarser than the clastic fraction of the
 279 organic-rich mud below and above. However, the clastic layers always contain a
 280 fraction of organic matter, too. The magnetic susceptibility signal of these layers
 281 ranges from relatively low, with values between 40 and 100 × 10⁻⁵ SI, to relatively
 282 high, with values up to 500 × 10⁻⁵ SI and higher (Fig. 4 and 5). The clastic layers are
 283 often visually indistinguishable from the organic-rich mud on the split core surface,
 284 except for black to brown colour contrasts. CT-scans of the clastic layers reveal sharp
 285 lower contacts with the highest radiodensity at the base, gradually decreasing upwards
 286 (Fig. 5a, b). Some clastic layers bear 1 to 3 cm large mud clasts in a matrix of sand or
 287 silt. The mud clasts have lower radiodensity than the matrix and are discernible on
 288 CT-scan as darker bodies (Fig. 5b). The mud clasts were difficult to impossible to
 289 identify on split core surfaces except for clastic layer cN. All other mud clasts were
 290 identified on X-ray CT-scans. If the clastic layers are brown, then they often coincide
 291 with a sharp colour transition from black to brown at their base. Some clastic layers
 292 have recognisable characteristics, e.g. thickness, colour, shape of the magnetic

293 susceptibility log etc. that can be traced laterally throughout the basin. This way the
 294 easiest-to-trace clastic layers were correlated, helping with the correlation of the other
 295 clastic layers.

296 The clastic layers are labelled from cA to cO, where “c” stands for Lake Cucao and
 297 the capital letter is in alphabetical order down core. This is in analogy to the Lake
 298 Huelde record 2 km north of Lake Cucao, where similar layers interpreted as tsunami
 299 deposits, are labelled hC, hD, and so on to hQ (Kempf et al., 2017). The topmost
 300 clastic layer in Lake Cucao was identified in Kempf et al. (Kempf et al., 2015) as the
 301 tsunami deposit of the CE 1960 tsunami and will be called CE 1960, instead of cA.



302
 303 *Figure 6: Seismic to core correlation of the CE 1960 tsunami deposit (cA) and clastic*
 304 *layers cB to cN (cO not represented on this figure) with strong acoustic*
 305 *reflectors R1 to R6. The assumption of uniform p-wave velocity within the entire*
 306 *lake infill and the piston coring process can cause minor offsets between cores*
 307 *and acoustic reflectors on sub-bottom profiles.*

308 Seven of 9 long cores contain the clastic layer cN in the lowest part of the
 309 sedimentary record, which is markedly coarser (fine to medium sand) and exhibits
 310 higher magnetic susceptibility values than the other clastic layers, with peaks up to
 311 2500×10^{-5} SI. Like in all other clastic layers, the sand of cN does not contain mica.
 312 The lack of mica distinguishes the sand of the clastic layers from the sand in samples
 313 from the tidal delta and the crosscutting channel (Kempf et al., 2015). In cN, intervals
 314 of well-sorted massive sands are intercalated with intervals of mud clasts in a sandy
 315 matrix. The mud clasts can exceed the size of the core liner (6 cm) and are up to 11
 316 cm thick. Smaller mud clasts are often arranged along horizons (Fig. 5c). Based on
 317 the radiodensity of the mud clasts, two types can be differentiated; one type with a

318 low radiodensity (black) and one type with an intermediate radiodensity (dark grey)
319 (Fig. 5c). The sand of the matrix and intervals of massive sand contain grains of
320 orthoclase, plagioclase, quartz, iron oxides (responsible for the high magnetic
321 susceptibility), hornblende and rarely zircon, as well as lithic grains. The same
322 composition of sand is reported for the CE 1960 deposit in Lake Cucao and Lake
323 Huelde and for the beach sand and dunes sand between Lake Cucao and the Pacific
324 Ocean (Kempf et al., 2015).

325 Three cores (Pos02, Pos03 and Pos11) contain poorly sorted, muddy sand at their base
326 (Fig. 4). The muddy content makes this sand distinctly different in grain size from the
327 well-sorted sand in the coarser clastic layers, e.g. clastic layers cC and cN. It consists
328 of the same minerals and lithic grains as the sand on the tidal delta and in the channel.

329 ***4.3 Sub-bottom profiles to core correlation***

330 Six of the long cores were projected on sub-bottom profiles that show acoustic
331 penetration of the entire seismic unit U2 (Fig. 6). The correlation between cores and
332 the sub-bottom profiles is performed under the assumption of a constant p-wave
333 velocity in the entire sedimentary sequence and no vertical deformation during
334 hammer-driven piston coring and then tying key marker layer with the sub-bottom
335 profile. Realistically, variability in p-wave velocity is expected to produce minor
336 offsets. The vertical deformation during hammer coring will cause net compression
337 and wave action on the lake while coring can cause extension, which will likely be
338 heterogenous and may produce significantly larger offsets. Some offsets are indicated
339 on the sub-bottom profiles to core correlation (Fig. 6).

340 The six reflectors of U2 (R1 to R6) can all be confidently correlated to clastic layers
341 in the cores (Fig. 4). The top of the CE 1960 tsunami deposit is buried by ≤ 3 cm of
342 lacustrine sediment in the western part of Lake Cucao (Kempf et al., 2015), which is
343 below the vertical resolution of the sub-bottom profiles (vertical resolution between
344 10 and 20 cm). R1, the uppermost strong reflector therefore correlates to the lake
345 floor as well as the top of the CE 1960 tsunami deposit. R2 correlates to clastic layer
346 cB. However, R2 is so close to the lake floor and R1 reflection, that interference of
347 reflections may lead to a poor identification of R2 in most cases. R3 correlates to cC,
348 R4 to cF and R5 to cJ, which are major traceable clastic layers in the sedimentary
349 record of Lake Cucao. They tend to be especially thick and coarse, and are
350 represented in most or all cores containing that specific stratigraphic interval. R6 is
351 the reflector that sticks out, because reflectors R2 to R5 on-lap to it. Even though a
352 spatial feature such as on-lapping is difficult to observe by comparison of multiple
353 cores, clastic layers cF to cM appear to on-lap to cN (Fig. 4). Because of its
354 stratigraphic position, the on-lapping and the strong sedimentary contrast between
355 organic-rich mud and the medium sand of clastic layer cN, we correlate the high-
356 amplitude reflector R6 to the coarse clastic layer cN (Tab. 2).

357

358 *Table 2: Summary of confidence levels for the interpretation of tsunami deposits for*
 359 *each clastic layer in Lake Cucao, with age and age-correlation to a known*
 360 *tsunami, maximum magnetic susceptibility, traceability of the clastic layers*
 361 *throughout the sedimentary record, correlation to acoustic reflections and*
 362 *content of mud rip-up clasts.*

event name	median age (95% age interval) yrs BP	potential age- correlation to published tsunami deposits	max. magnetic susceptibility (10 ⁻⁵ SI)	traceability in the sedimentary record represented in cores/cores reaching this depth interval	correlated to acoustic reflector	mud rip-up clasts	confidence level
cA/CE 1960	-7 (-11 to -5)	yes	677	18/18	R1	yes	high
cB	287 (185 - 418)	yes	695	17/17	R2	yes	high
cC	1081 (894 - 1274)	maybe	1601	9/9	R3	yes	high
cD	1226 (1031 - 1418)	yes	57	5/8	-	not observed	medium
cE	1274 (1079 - 1466)	maybe	51	2/8	-	not observed	low
cF	1656 (1454 - 1656)	yes	581	8/8	R4	yes	high
cG	1825 (1624 - 1986)	yes	431	7/8	-	not observed	medium
cH	1962 (1765 - 2109)	yes	202	5/8	-	not observed	medium
cI	2099 (1914 - 2213)	no	335	5/8	-	not observed	medium
cJ	2254 (2077 - 2322)	yes	306	8/8	R5	yes	high
cK	2530 (2378 - 2662)	yes	377	7/7	-	yes	high
cL	2883 (2670 - 3001)	no	92	3/7	-	not observed	low
cM	3699 (3530 - 3906)	yes	585	4/4	-	yes	high
cN	3783 (3612 - 3994)	yes	2269	8/8	R6	yes	high
cO (in model)	3798 (3626 - 4011)	no	1656	3/3	-	not observed	medium
cO (corrected)	4101 (3959 - 4344)	"	"	"	"	"	"

363

364 **4.4 Age control**

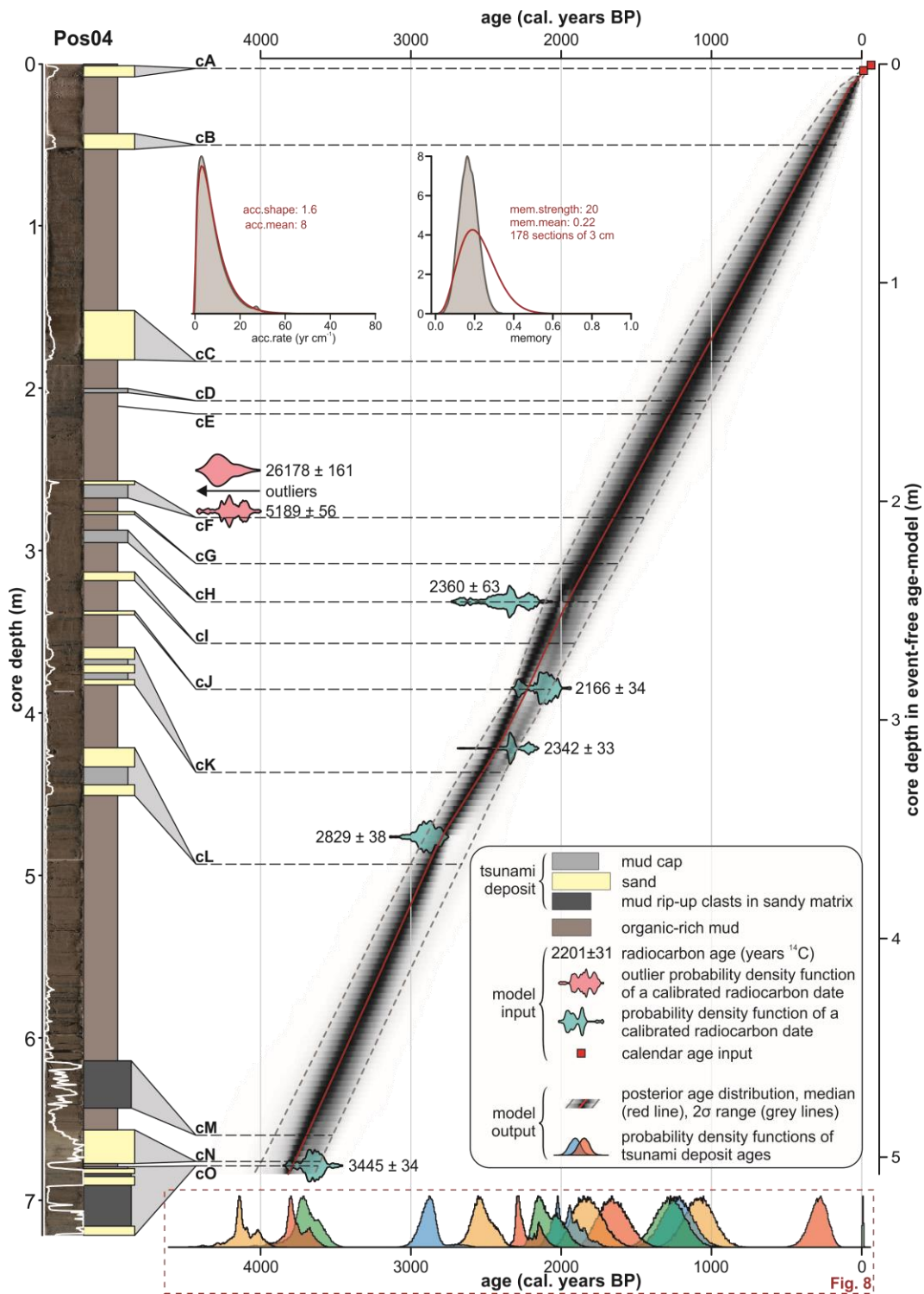
365 The clastic layers exhibit characteristics of abrupt deposition, e.g. sharp lower
 366 contacts, mud clasts and decreasing upwards radiodensity, which often reflects fining
 367 upwards (cf. [Van Daele et al., 2014](#)). The intervals of the clastic layers are therefore
 368 likely to have been deposited with a different accumulation rate from the rest of the
 369 sedimentary record, most likely quasi-instantaneously.

370 We used composite core Pos04 to develop an age-depth model for Lake Cucao. The
 371 prior age-depth information consists of the following data and considerations:

- 372 i) radionuclide data that identified the CE 1960 tsunami deposit ([Kempf et](#)
 373 [al., 2015](#))
- 374 ii) 7 radiocarbon dates ([Tab. 1](#))
- 375 iii) clastic layers were treated as instantaneous deposits, i.e. they were taken
 376 out of the core for age-depth modelling
- 377 iv) the sediment is a lacustrine sedimentary sequence, so we assume a
 378 relatively stable sedimentation. This is supported by the uniform nature of
 379 the sediment sequence with parallel reflections on sub-bottom profiles at
 380 the core site.

381 All age-depth information of Pos04 was fed into the autoregressive Bayesian age-
 382 depth modelling algorithm BACON ([Blaauw and Christen, 2011](#)). The parameters
 383 were adjusted to divide the core into 178 sections of 3 cm and to reflect the relatively

384 stable lake environment, i.e. continuous sedimentation of the organic-rich lacustrine
 385 mud (Fig.7).



386
 387 *Figure 7: Bayesian age-depth model of core Pos04 in Lake Cucao calculated with*
 388 *BACON (Blaauw and Christen, 2011). The core surface image and*
 389 *sedimentological core log are displayed on the left. The tsunami deposits are*
 390 *treated as instantaneous deposits and are taken out of the core for age-depth*
 391 *modelling. The bottom x-axis shows the model results for all tsunami deposits as*
 392 *coloured age distributions.*

393 The model output shows that there are two obvious outliers, i.e. extreme age
394 reversals, among the radiocarbon dates (samples CUCA10B-1.5 and CUCA10B-51),
395 which were neglected by the age-depth algorithm for making the age-depth model.
396 From the resulting age-depth model we extracted the age probability distributions of
397 all clastic layers that were treated as instantaneous deposits (Fig. 7). The problem
398 connected to the relatively long interval of interpolation between the core top and the
399 shallowest radiocarbon date (2360 ± 63 yrs BP) is minimised by the relatively stable
400 sedimentary environment at core site Pos04.

401 The assumption of relatively stable accumulation rates in Pos04 (iv) appears to fail
402 only at the lowest end of the sedimentary record (between clastic layers cN and cO).
403 This becomes evident when comparing the 2 cm thick organic-rich mud interval in
404 core Pos04 with the 43.5 cm thick organic-rich mud interval of the same stratigraphic
405 position in core Pos06. The age-depth model on core Pos04 likely underestimates the
406 time difference between clastic layers cN and cO. Using the average accumulation
407 rate of the entire record down to clastic layer cN of ~ 1.31 mm yr⁻¹ (502 cm of
408 sediment accumulation in 3845 years), clastic layer cO is probably ~ 330 years older
409 than clastic layer cN.

410 5 Discussion

411 5.1 Antidunes as a product of tsunami inundation in Lake Cucao

412 The hummocks with the up-slope dipping internal reflectors underneath R4 (clastic
413 layer cF) are interpreted as antidunes due to their height and length in combination
414 with the up-slope dipping internal reflectors. Antidunes form in the upper stage
415 supercritical flow regime. The wavelength of antidunes is related to the wavelength of
416 the standing wave that produced them (Allen, 1984), which in turn is proportional to
417 the square of the flow speed during formation (Kennedy, 1963). The resulting
418 relationship between flow speed and wavelength of the antidune bedform is described
419 by Carling (2009) with

$$420 \quad U = \sqrt{\frac{g L_a}{2\pi}} \quad (1)$$

421 Where U is the flow speed, g the gravitational acceleration on earth and L_a the
422 average wavelength in a train of antidune bedforms. The flow depth d in dependence
423 on average wavelength is expressed by

$$424 \quad d = \frac{L_a}{2\pi} \quad (2)$$

425 According to equation (1) the flow speed during antidune formation was ~ 6.8 m s⁻¹
426 (24.6 km h⁻¹) and according to equation (2) the flow depth was ~ 4.8 m. Both
427 dimensions compare well with directly measured flow properties of recent large-scale
428 tsunami inundations (cf. Fritz et al., 2012). The location of the antidunes suggests that
429 the freshwater marsh, which now accommodates most inhabitants of the village of
430 Cucao was washed over by strong, certainly destructive water currents. Despite their
431 size, antidunes form relatively quickly once supercritical flow develops. However,

432 with three antidunes of similar shape and size, we argue that supercritical flow was
433 well developed, steady and sustained.

434 *5.2 Age control and accumulation rate variability in Lake Cucao*

435 There is no overall strong spatial variability in accumulation rate between long cores
436 from the western part of the basin, which is indicated by sub-parallel clastic layers in
437 the core to core correlation. This is confirmed by parallel to sub-parallel reflectors R1
438 to R5 on sub-bottom profiles (Fig. 2a, b).

439 There are three exceptions, which are

- 440 i) confined areas of erosional truncation in form of small channels (Fig. 2c),
- 441 ii) the area close to the crosscutting channel along the north-eastern side of
442 the lake, where the sedimentary infill becomes significantly thinner or is
443 non-existent (Fig. 2c, d), and
- 444 iii) the deepest part of most long cores, where the strata form on-laps (this
445 includes the age-depth modelled core Pos04 between cN and cO).

446 All long core sites avoid the areas of i) and ii).

447 In short cores CUC10 and CUC11, located 2–3 km southeast of most other cores (Fig.
448 4), and where tidal currents are probably weaker or absent, up to 21 cm of organic-
449 rich mud accumulated above the CE 1960 tsunami deposit. This thickness is
450 comparable to 20–30 cm of post-1960 sediment accumulation in Lake Huelde (Kempf
451 et al., 2015), which is currently unaffected by tidal currents. In all other cores further
452 west in Lake Cucao the same interval is either ≤ 4 cm thick or missing, showing non-
453 deposition or episodes of erosion in the post-1960 lake environment in the ocean-
454 proximal area of the lake.

455 The age-control of the last 2000 yrs relies strongly on the assumption of stable
456 accumulation rates between the CE 1960 tsunami deposit and the uppermost useful
457 radiocarbon date at 246 cm (event-free core depth) (Fig. 7, Tab. 1). Cores and sub-
458 bottom profiles justify this interpolation, because of the uniform stratigraphy with
459 little lateral variability in this part of the stratigraphic record of U2 near the coring site
460 Pos04.

461 Chronologies of other regional paleotsunami and paleoseismic records from south
462 central Chile are based on similar primary age-depth information, i.e. on radiocarbon
463 dates of plants flattened by the tsunami, rootlets in soil, terrestrial plant fragments
464 from the pre- and post-tsunami lacustrine sediment and tephra (Atwater et al., 2013;
465 Cisternas et al., 2017, 2005; Garrett et al., 2015; Kempf et al., 2017; Moernaut et al.,
466 2018, 2014). The uncertainty intervals of tsunami ages in the Lake Cucao record are
467 greater than the uncertainty intervals of the tsunami ages of, for example, the
468 paleotsunami record of Lake Huelde. Nevertheless, the Lake Cucao ages correlate
469 well with regional paleotsunami records (Fig. 8). The age-control can be considered
470 of comparable quality.

471

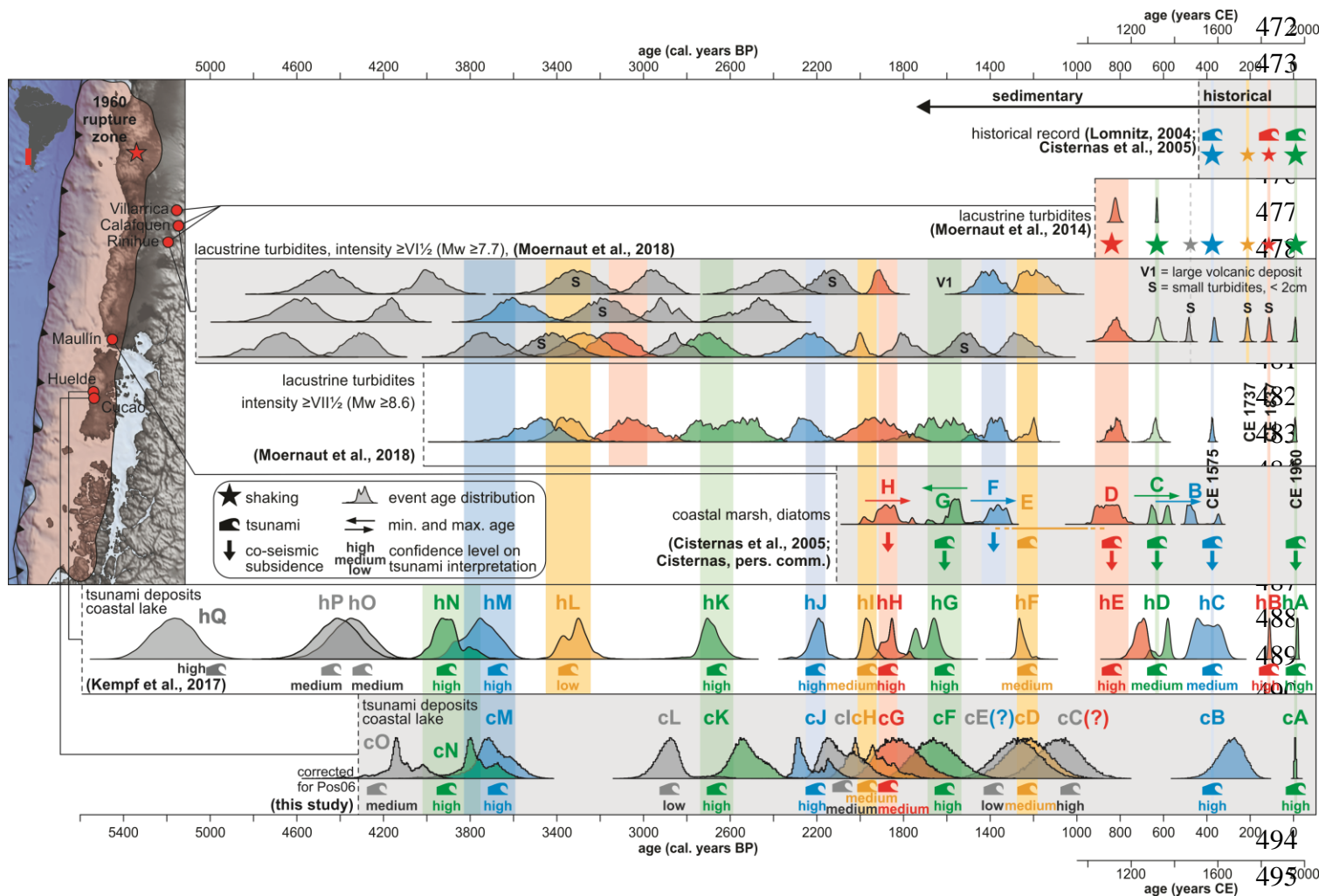


Figure 8: Regional correlation of paleoseismic and paleotsunami records. The instrumental record only includes the CE 1960 event and is not especially listed here. Documented history reveals three more large events in CE 1575, 1737, 1837 (Cisternas et al., 2005; Lomnitz, 2004). Lacustrine turbidites from the Chilean lake district give paleoseismic evidence (Moernaut et al., 2018, 2014). The paleotsunami records from Maullín (Cisternas et al., 2005) and Lake Huelde (Kempf et al., 2017) offer the direct comparisons between

496 tsunami deposits. The age of cO is here corrected by 330 yrs because of the regular organic-rich lacustrine sediment between cN and cO in core
 497 Pos06 (in contrast to core Pos04 for which the age-depth model was made).

498 ***5.3 Age of the crosscutting channel and constraints on Lake Cucao's vertical***
499 ***displacement history***

500 Coastal areas on subduction zones are known to be prone to vertical deformation
501 throughout the seismic cycle (Wesson et al., 2015). The CE 1960 Great Chilean
502 Earthquake caused the area around Lake Cucao to subside co-seismically by ~1 m
503 (Plafker and Savage, 1970), which put Lake Cucao into an intertidal position, if the
504 lake level was not already in the intertidal zone before. The subsidence of ~1 m may
505 have intensified the tidal currents, which would explain the limited post-CE 1960
506 sedimentation in all but the most distal coring sites. The tidal currents entering the
507 lake during high tide are continuing to form the intertidal delta, the crosscutting
508 channel and the mega-ripples. Given that the sedimentary record below the CE 1960
509 tsunami deposit appears to have stable accumulation rates, we argue that the vertical
510 position of the river channel in relation to the relative sea level is probably at an
511 extreme low at present in respect to the last 4300 yrs.

512 If the channel would be a recently formed feature, it would truncate the mostly
513 parallel to sub-parallel internal reflectors of seismic unit U2. This is not the case; all
514 internal reflectors, R1 to R5, in U2 converge towards the channel (Fig. 2c), which
515 indicates that intertidal currents were active at least episodically during the period
516 represented by the sedimentary infill visible on sub-bottom profiles. This constrains
517 the net vertical displacement of Lake Cucao in the last 4300 yrs to a narrow window
518 around its current position.

519 Additionally, river channels play a primary role in connecting the ocean with coastal
520 lakes during tsunami inundation (Kempf et al., 2017, 2015). Consequently, regardless
521 of the exact position of the coastline and river channel migrations, Lake Cucao may
522 have been a reliable tsunami recorder with relatively stable sensitivity to tsunami
523 inundation in the past 4300 yrs and potentially longer.

524 ***5.4 Identifying tsunami deposits in the Lake Cucao sedimentary record***

525 The clastic layers share similar sedimentary characteristics to the tsunami deposit of
526 CE 1960. However, other causative processes must be excluded before a tsunami
527 origin can be assigned. Tsunami deposits have several sedimentary characteristics,
528 most are site-specific, and few are unique to tsunami deposits. For example,
529 landwards thinning and landward fining sand sheets can be produced by storm surges
530 and tsunamis alike (Kortekaas and Dawson, 2007). However, the relatively distant
531 inland location (~1.3 km between ocean and lake) makes storm deposition in Lake
532 Cucao unlikely. While storms occur on the south central Chilean coast, the tropical
533 cyclones with the potential to create deposits kilometres inland and in coastal lakes,
534 have not been documented and are unlikely to happen, even under strong El Niño
535 conditions (Fedorov et al., 2010).

536 Excluding competing hypotheses for the formation of similar layers is equally
537 valuable. For Lake Cucao we can, for example, exclude flood turbidites, which are
538 not uncommon in Chilean lakes (e.g. Van Daele et al., 2019), because upstream

539 adjacent Lake Huillinco traps riverine flood input to Lake Cucao, which reduces the
540 direct riverine input to Lake Cucao to a small creek that enters Lake Cucao from the
541 south in its eastern part. The small creek does not have a large enough catchment to
542 produce lake-wide flood turbidites. And if it were to produce flood turbidites the
543 fining of sediment would be away from the inflow of the creek, i.e. east to west in the
544 study area and not west to east.

545 We define the following five criteria for the sedimentary environment of Lake Cucao,
546 which are either indicative of tsunami deposition or can be used to exclude other
547 processes.

548 i) *High magnetic susceptibility* – Magnetic susceptibility is controlled by the
549 ferrimagnetic mineral content of the sediment. High magnetic susceptibility in
550 Lake Cucao means the sediment contains iron oxides (i.e. hematite and
551 magnetite). The concentrations of ferrimagnetic minerals in the basin of Lake
552 Cucao can be increased by organic matter depletion, compaction or by
553 deposition of iron oxides. The low magnetic susceptibility values of organic-
554 rich mud and the sometimes extremely high values of magnetic susceptibility
555 in the clastic layers suggest that the layers with high magnetic susceptibility
556 values are from extra-lacustrine sources. Processes that could provide such a
557 sediment source are limited to lake-inundating events, such as storms and
558 tsunamis. This effect has been described for the CE 1960 tsunami deposit
559 ([Kempf et al., 2015](#)).

560 ii) *Traceability in the sedimentary record* – Tsunami deposits in coastal lakes are
561 spatially variable in thickness ([Kelsey et al., 2005](#); [Kempf et al., 2017](#)).
562 However, tsunami deposits are often continuous deposits to where they wedge
563 out towards their maximum lateral extent. When tsunamis inundate coastal
564 lakes, the water flow contains and deposits sand, remobilises muddy lake
565 sediment and redistributes it within the lake basin. Areas beyond the zone of
566 sandy deposition can receive exclusively muddy tsunami sediment ([Kelsey et al., 2005](#); [Kempf et al., 2017, 2015](#)). Therefore, tsunami deposits should be
567 traceable in the sedimentary record throughout large areas of the lake, if not
568 the entire lake basin. The criterion is given as a fraction of the number of
569 cores, in which the clastic layer is observed over the number of cores, in
570 which the stratigraphic interval of the clastic layer in question was recovered.
571 Complete or nearly complete representation in the sedimentary archive is
572 treated as indicative for tsunami deposition ([Fig. 4](#)).

574 iii) *Acoustic reflector correlation* – The six strong reflectors (R1–R6) on the sub-
575 bottom profiles represent strong contrasts in acoustic impedance, i.e.
576 differences in p-wave velocity and/or density. In an organic-rich mud-
577 dominated environment high acoustic impedance contrast can be associated
578 with clastic layers. Not every clastic layer will necessarily produce a high-
579 amplitude reflector, but if a clastic layer can be correlated to a basin-wide
580 high-amplitude acoustic reflector, then this points towards basin wide

581 distribution and high clastic content, which is expected from a tsunami
582 deposit.

583 iv) *Mud rip-up clasts* – We interpret the mud clasts as mud rip-up clasts. Mud rip-
584 up clasts are generated by high-energy processes in otherwise low-energy
585 environments. In sub-aquatic landslides, mud rip-up clasts occur on the
586 spectrum of disintegration of the sliding sediment from slumps, to debris
587 flows, to turbidity currents (cf. Lee et al., 2013). Onshore landslides that
588 impact muddy fjord sediment have also produced mud rip-up clasts, which
589 may show paleo flow direction by imbrication (Van Daele et al., 2014). In
590 fluvial systems mud rip-up clasts are associated with cut bank collapses of
591 muddy soils. In coastal environments, like marshes, mud rip-up clasts are
592 commonly associated with tsunami deposition (Peters et al., 2007), however,
593 storm surges reportedly can produce mud rip-up clasts, too (Phantuwongraj et
594 al., 2013). In Lake Cucao, two types of mud rip-up clasts can be differentiated
595 by their radiodensity. One type has the same radiodensity as the lacustrine
596 organic-rich mud and is interpreted as such. The other type has higher
597 radiodensity and could represent soil from the lake-surrounding marshes.
598 Similar variations in mud rip-up clasts were described in trenches on the
599 Chilean main land near Maullín (Atwater et al., 2013). Specifically for Lake
600 Cucao, the presence of both types of mud rip-up clasts excludes strong tidal
601 currents and slope failure turbidites. Tidal currents could work similarly to
602 fluvial systems with regard to the erosional process for the source material of
603 mud rip-up clasts and to the depositional process of clastic layers.

604 v) *Age-correlation* – Megathrust earthquake-induced tsunamis hit long stretches
605 of coastline. Tsunami deposits can be correlated over long distances using
606 their chronology (Cisternas et al., 2017; Peters et al., 2007). If a clastic layer
607 correlates in age to an identified tsunami deposit elsewhere in south central
608 Chile, then this corroborates the interpretation as a tsunami deposit. In the
609 Lake Cucao sedimentary record, the interpretation of the CE 1960 tsunami
610 deposit was partially based on such an age correlation. Downcore, age-
611 correlation with the Lake Huelde sedimentary record (Kempf et al., 2017) is
612 especially interesting, because of the lakes' proximity (2 km) to each other and
613 the similarity of the paleotsunami record, despite the difference in lacustrine
614 sedimentary environments.

615 Two of the 15 clastic layers (cE, and cL) fulfil only one or no criterion at all. The
616 confidence of an interpretation as a tsunami deposit in these cases is low, however, a
617 tsunami origin is probably still the most favourable hypothesis (Tab. 2). Eight clastic
618 layers fulfil three or more criteria and the confidence level for interpreting these
619 layers as tsunami deposits is high. The remaining 5 clastic layers fulfil two criteria
620 sufficiently and receive a medium confidence level.

621 The Lake Cucao record potentially matches with 10 regionally known paleotsunami
622 and paleoseismic events (Fig. 8, Tab. 3). Additionally, deposit cC matches to some
623 extent with deposit hE in Lake Huelde and event D in Maullín, but weaker age control

624 in the Lake Cucao record for the last ~2000 yrs may inhibit a conclusive correlation.
 625 The confidence level for both event deposit hE and cC are high, which supports the
 626 hypothesis of same origin, because in no other instance is there a high confidence
 627 tsunami deposit in Lake Huelde without a matching tsunami deposit in Lake Cucao
 628 and vice versa. The only exception is the cryptic CE 1837 tsunami deposit, that was
 629 recognised in Lake Huelde by IRSL dating (Kempf et al., 2015).

630 *Table 3: Regional age-correlation of paleotsunami and paleoseismic events.*

historical record	Cucao	Huelde	Mauullín	Rinihue Calafquen Villarrica
year of event	name in record (confidence level)	name in record (confidence level)	name in record	correlating event
1960	cA (high)	hA (high)	A	yes
1837	-	hB (high)	-	yes
1737	-	-	-	yes
1575	cB (high)	hC (medium)	B	yes
beyond record	-	hD (medium)	C	yes
	cC (high) (?)	hE (high)	D	yes
	cD (medium)	hF (medium)	E	yes
	cE (low) (?)	-	F	(?)
	cF (high)	hG (high)	G	yes
	cG (medium)	hH (high)	H	yes
	cH (medium)	hI (medium)	beyond record	yes
	cl (medium)	-		(?)
	cJ (high)	hJ (high)		yes
	cK (high)	hK (high)		yes
	cL (low)	-		no
	-	hL (low)		yes
	cM (high)	hM (high)		yes
	cN (high)	hN (high)		(?)
	cO (medium)	-		(?)
	beyond record	hO (medium)		(?)
		hP (medium)		(?)
		hQ (high)		beyond record

631

632 Deposit cE matches well with event F in Mauullín, however, Lake Huelde does not
 633 record tsunami deposition in this period and in Mauullín the event was only recognised
 634 by co-seismic subsidence and not with a tsunami deposit (Tab. 3) (Cisternas et al.,
 635 2005; Kempf et al., 2017). Either Lake Cucao was relatively sensitive to tsunami
 636 inundation at the time and recorded a minor tsunami that had no sedimentary impact
 637 in Mauullín, Lake Huelde and other regional paleotsunami records. Or as the low
 638 confidence level denotes, deposit cE is potentially not a tsunami deposit.

639 Both deposits cL and hL have only a minor sedimentary imprint in Lake Cucao and
 640 Lake Huelde, respectively, with low confidence level on the interpretation as tsunami
 641 deposits (cf. Kempf et al., 2017). If either deposit is a tsunami deposit, then the origin

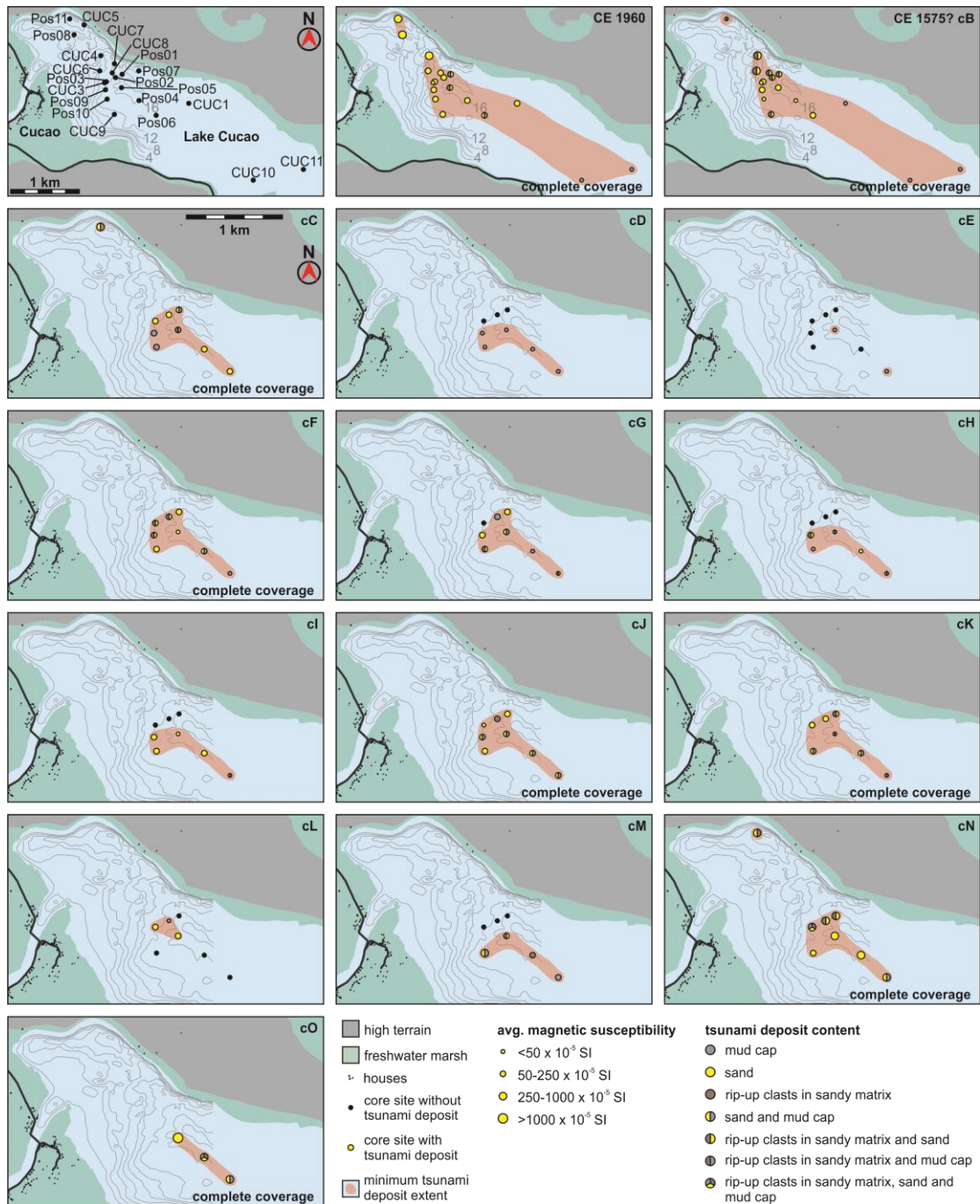
642 is probably a minor tsunami. The age-depth modelling in both records does not match
643 the two deposits, so that it can be concluded that they are most likely not from the
644 same event.

645 In contrast, for example, deposits cK and hK from Lake Cucao and Lake Huelde,
646 respectively, share a similar clear (high confidence level), but not extreme
647 sedimentary imprint in their respective records. The age-depth models match the two
648 deposits, so it is likely that cK and hK were deposited during the same tsunami
649 inundation event.

650 *5.5 Spatial perspective on tsunami deposits in a lake basin*

651 Event maps (Figs. 9 and 10) that summarise the sedimentary characteristics of the
652 tsunami deposits visualise spatial trends of the tsunami deposits. The following
653 conclusions are supported by the spatial data.

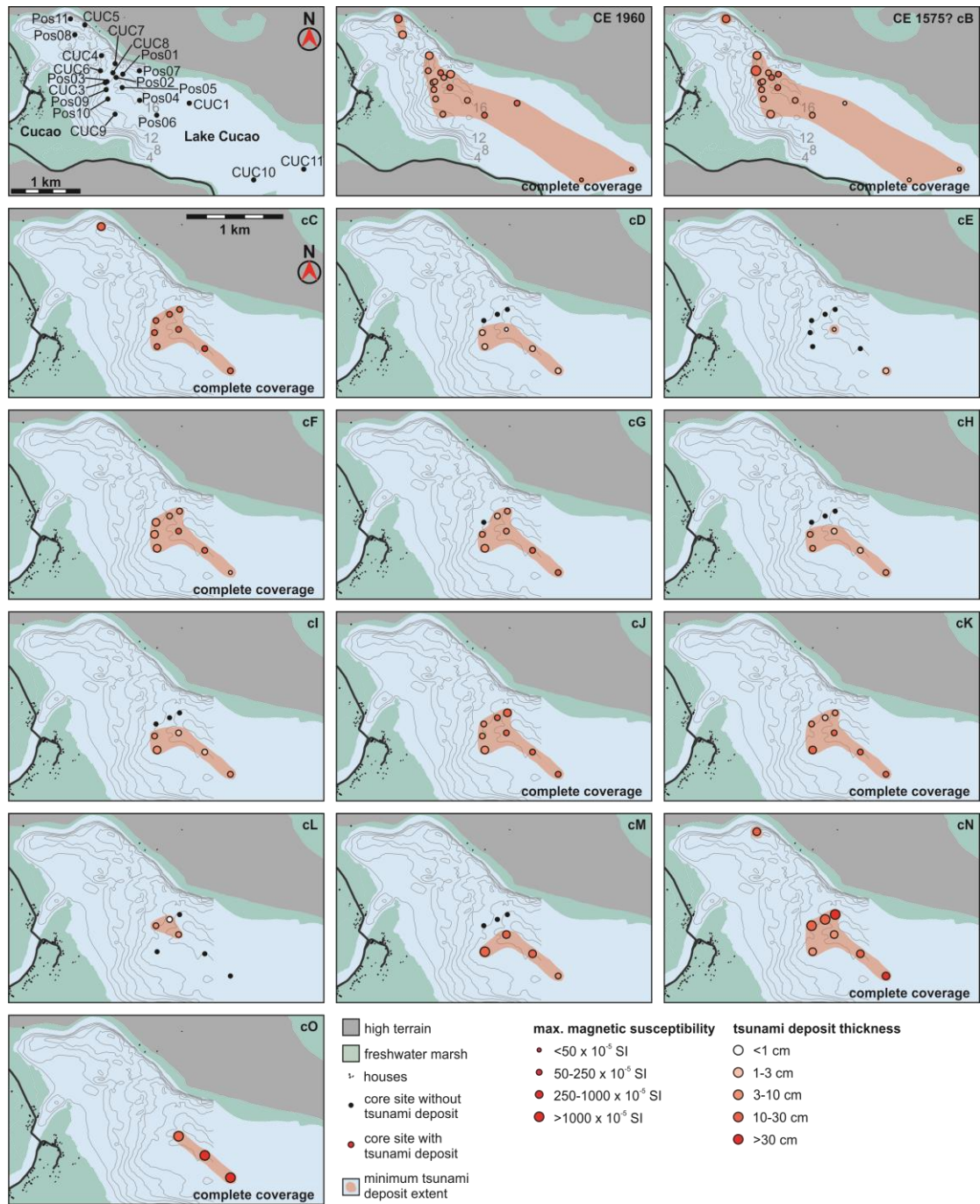
- 654 i) Mud rip-up clasts are limited to the proximal part of the lake basin (Fig.
655 9). The tsunami deposit cO at core site Pos04 is the only exception. This
656 trend seems plausible as it requires high energy water flow to erode and
657 transport mud rip-up clasts. Dissipating energy in the fluid flow over
658 distance would dictate that mud rip-up clasts would be the first particles to
659 resist transport or remobilisation.
- 660 ii) For a large extent in the lake basin, tsunami deposits do not decrease in
661 thickness. This contradicts the spatial trend in onshore tsunami deposits,
662 where tsunami deposit thickness is influenced by the onshore morphology
663 and tends to decrease with increasing run-up distance (Goto et al., 2014).
664 This study has thickness data along up to ~3 km of inundation distance.
665 Even for the tsunami deposit thickness data from CE 1960 and CE 1575
666 (cB) with a ~3 km long transect no decreasing trend in thickness can be
667 recognised. Logically, in the most distal parts of the record the tsunami
668 deposit must wedge out, however, the core sites are not located in the area
669 where this occurs.
- 670 iii) From the location where a tsunami deposit has a muddy component, the
671 muddy characteristic in the tsunami deposits is always present in more
672 distal locations. Examples are the tsunami deposits cF, cK or cM. This
673 highlights one aspect of the reliability of coastal lakes to record tsunami
674 deposits.
- 675 iv) To record tsunami deposition over large parts of a lacustrine basin, muddy
676 grainsizes can be sufficient, e.g. tsunami deposit cD (Fig. 9). However,
677 detection of those deposits is more difficult, because of the similarities to
678 the surrounding regular lacustrine sediment. In the case of the muddy
679 tsunami deposits in Lake Cucao the magnetic susceptibility was enough to
680 indicate candidate clastic layers. In environments, where magnetic
681 susceptibility cannot be used, other methods need to be tested, e.g. XRF
682 scanning or a bio-marker analysis.



683

684 *Figure 9: Event map of all tsunami deposit cA, i.e. CE 1960, to cO. The dots refer to*
 685 *core sites that contain the stratigraphic interval in which the tsunami deposit is*
 686 *located. Black dots mean the tsunami deposit was not detected. The size of the dot*
 687 *is a function of the average magnetic susceptibility over the entire tsunami*
 688 *deposit. The colour of the dot is a function of the sedimentary content of the*
 689 *tsunami deposit. The red polygon depicts the lateral extent of the tsunami deposit.*

690



691

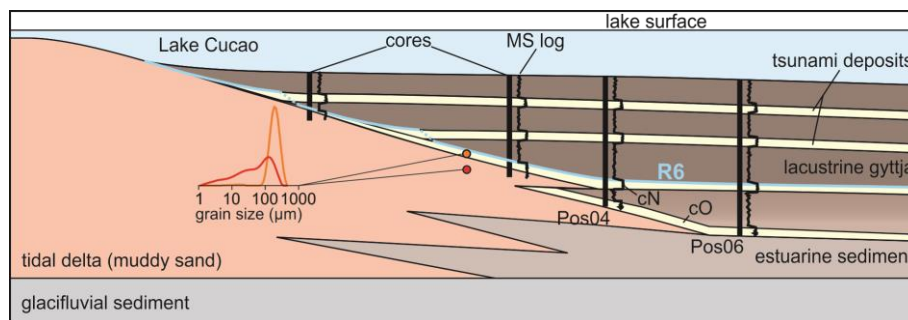
692 *Figure 10: Event map of all tsunami deposit cA, i.e. CE 1960, to cO. The dots refer to*
 693 *core sites that contain the stratigraphic interval in which the tsunami deposit is*
 694 *located. Black dots mean the tsunami deposit was not detected. The size of the*
 695 *dot is a function of the maximum magnetic susceptibility of the tsunami deposit.*
 696 *The colour of the dot is a function of the tsunami deposit thickness in the core*
 697 *(darker red means thicker tsunami deposit). The red polygon depicts the lateral*
 698 *extent of the tsunami deposit.*

699

700 **5.6 A conceptual model towards the origin and evolution of the lake basin**

701 In order to contrive a conceptual stratigraphic model of Lake Cucao that incorporates
702 all sedimentologic evidence available, we begin with the topographical depression
703 that is now occupied by Lake Cucao. The depression was a glacifluvial river valley
704 (Glasser et al., 2008), which was submerged during the last global post-glacial
705 eustatic sea-level rise (Siddall et al., 2003). During this transgression, the glacifluvial
706 valley must have become an estuary, a similar evolution to lakes Lanalhue and Lleu
707 Lleu ~500 km further north (Fig. 1) (Stefer et al., 2010). The oldest recovered
708 sediment in core Pos04 (around tsunami deposit cN, reflector R6) is lacustrine,
709 indicating that the barrier, which makes Lake Cucao a coastal lake, rather than an
710 estuary, has been in place earlier than 4300 yrs ago.

711 Most likely aeolian sediments silled off the estuary and created the barrier and
712 therewith the enclosed lake basin. The timing of the sill formation is unclear,
713 however, one plausible hypothesis is that the expanding westerlies between 8.5 and
714 5.5 ka (Lamy et al., 2010) may have enabled aeolian processes to create the sill.
715 Aeolian processes are still prevailing in the coastal area west of Lake Cucao
716 evidenced by an active dune belt.



717

718 *Figure 11: Conceptual stratigraphic model of Lake Cucao's sedimentary infill that*
719 *summarizes the sedimentologic evidence available in the literature and in the*
720 *results of this study. This model also explains the corrected age of tsunami*
721 *deposit cO.*

722 Currently, Lake Cucao lies in the intertidal zone (Kempf et al., 2015; Villalobos et al.,
723 2003), with saline water flowing into the lake from the Pacific during high tide. This
724 process has been active at least sporadically since 4300 cal. yrs BP, evidenced by the
725 convergent internal reflectors in the entire sediment sequence of U2 near the tidal
726 channel. The same process has built up a tidal delta in Lake Cucao around the outlet.
727 The conceptual stratigraphic model includes foresets of the tidal delta interfingering
728 with lake basin and estuarine sediments (Fig. 11). One of these foresets may explain
729 the muddy sand with the same characteristics as the exposed tidal delta sediments at
730 the base of cores Pos02, Pos03 and Pos11. Clastic layer cN, interpreted as a tsunami
731 deposit, is in direct contact to the muddy sand in all cores of the western part of the
732 basin, except at Pos06. It appears that the formation of cN disrupted the deposition of
733 muddy sand at the mentioned core locations. Clastic layer cN is thicker and coarser
734 than all other clastic layers in most core locations. Additionally, the deposit correlates

735 chronologically to deposit hN, which is among the thicker and coarser tsunami
736 deposits from the nearby Lake Huelde paleotsunami record (Kempf et al., 2017).

737 The overall extreme character relative to other tsunami deposits in the respective
738 records of cN and hN may point towards an unusually strong tsunami. The end of
739 foreset sedimentation after deposition of cN could be due to a large amount of either
740 co-seismic uplift or subsidence during this event.

741 In the uplift scenario the lake system may stop interacting with the Pacific Ocean
742 altogether. Tidal inflows into the lake would not occur and the processes, which form
743 topsets and foresets on the tidal delta, would stop. Large amounts of co-seismic uplift
744 can occur on the Chilean coast, e.g. in CE 1960 on Isla Guafo (Sievers et al., 1963).
745 However, the geometry of the crust on and off Chiloé Island probably needs splay
746 fault slip to generate such an uplift and an outstanding tsunami, as neither CE 1960,
747 1837 nor 1575 created large co-seismic uplift there (Cisternas et al., 2017; Garrett et
748 al., 2015; Plafker and Savage, 1970; Sievers et al., 1963).

749 The subsidence scenario seems more plausible, because of the example given by co-
750 seismic subsidence around Cucao (~1 m) during the CE 1960 earthquake (Plafker and
751 Savage, 1970). The subsidence would create accommodation, which would favour
752 aggradation at the cost of progradation of the delta. During aggradation on the delta,
753 the lake basin would accumulate organic-rich mud. Once aggradation used up the
754 newly available accommodation, the lake system would switch back to progradation
755 and begin forming the next interfingering foreset. In both examples, the presence of
756 the tidal delta would be less dominant in the basinal sediments.

757 **6 Conclusions**

758 Based on sub-bottom profiles and numerous sediment cores, we add a new, long and
759 continuous paleotsunami record in the rupture zone of the CE 1960 Great Chile
760 Earthquake. We present following conclusions:

- 761 i) Sub-bottom profiles are crucial to understand the dynamic sedimentary system
762 of coastal lakes and to help in selecting the most appropriate coring locations
763 for paleotsunami research. Moreover, sub-bottom profiles may reveal
764 sedimentary structures which can allow quantification of flow speed and
765 depth, e.g. antidunes (Fig. 2).
- 766 ii) Dynamic coastal lakes with daily tidal inflow can be used for extracting long
767 paleotsunami records. For the last 4300 yrs, Lake Cucao presents 15 tsunami
768 deposits of mostly moderate to high confidence on the interpretation. This
769 confidence level was based on physical sedimentary characteristics and
770 contextual characteristics (Tab. 2), such as maximum magnetic susceptibility,
771 traceability (Figs. 9 and 10), correlation to acoustic reflectors on the sub-
772 bottom profiles (Fig. 6), the presence or lack of mud rip-up clasts (Figs. 5 and
773 9), and age correlation with regional paleotsunami (Fig. 8). At least 10
774 tsunami deposits correlate to paleotsunami deposits found in nearby Lake
775 Huelde.

- 776 iii) The most complete tsunami record was found in core Pos05, 1.3 km from the
777 lake outlet (tidal inlet) and a total 2.6 km from the present-day coastline. This
778 relatively far inland location for regular tsunami deposition is facilitated by the
779 river channel. There is evidence for tidal currents throughout the entire record,
780 and thus persistent river connection, which allowed for continuous recording
781 of tsunamis, despite co-, post- and inter-seismic relative sea level change in
782 the late Holocene. However, such tidal currents can affect sediment dynamics,
783 leading to variable depositional rates in space and time, adding complexity for
784 reliable mapping and dating of tsunami deposits.
- 785 iv) This study underlines the many challenges and extraordinary advantages
786 associated to paleotsunami research on coastal lakes and demonstrates how
787 indispensable geophysical mapping and numerous coring sites are in
788 understanding the depositional environment of dynamic coastal lakes for
789 extracting high-quality, long and continuous paleotsunami records.

790 **Acknowledgments**

791 PK acknowledges financial support by the Special Research Fund of Ghent University
792 (BOF), JM from the Chilean Fondecyt projects nr. 1150346 and 1150321, MVD from
793 the Research Foundation Flanders (FWO travel grant K201512N), RU from
794 CONICYT/FONDAP/15130015. We thank Koen De Rycker, Willem Vandoorne and
795 Gauvain Wiemer for fieldwork support, Dr. Claire Schepens and Dr. Eric Achten for
796 CT-scanner support. IHS Markit is acknowledged for providing the Kingdom seismic
797 interpretation software within their educational grant program.

798 **References**

- 799 Allen, J.R.L., 1984. *Sedimentary Structures: Their Character and Physical Basis*.
800 Elsevier, Amsterdam.
- 801 Amante, C., Eakins, B.W., 2009. ETOPO1 1 Arc-Minute Global Relief Model:
802 Procedures, Data Sources and Analysis. NOAA Technical Memorandum
803 NESDIS NGDC-24. National Geophysical Data Center, NOAA.
804 doi:10.7289/V5C8276M
- 805 Atwater, B.F., Cisternas, M., Yulianto, E., Prendergast, A.L., Jankaew, K., Eipert,
806 A.A., Ignatius, W., Fernando, S., Tejakusuma, I., 2013. The 1960 tsunami on
807 beach-ridge plains near Maullín, Chile: Landward descent, renewed breaches,
808 aggraded fans, multiple predecessors. *Andean Geology* 40, 393–418.
809 doi:10.5027/andgeoV40n3-a01
- 810 Blaauw, M., Christen, J.A., 2011. Flexible Paleoclimate Age-Depth Models Using an
811 Autoregressive Gamma Process. *Bayesian Analysis* 6, 457–474. doi:10.1214/11-
812 BA618
- 813 Carling, P., Burr, D., Brennand, T.A., 2009. A review of open-channel megaflood
814 depositional landforms on Earth and Mars A review of open-channel megaflood
815 depositional landforms on Earth and Mars, in: Burr, D.M., Carling, P.A., Baker,

- 816 V.R. (Eds.), *Megaflooding on Earth and Mars*. pp. 33–49.
817 doi:10.1017/CBO9780511635632.003
- 818 Chagué-Goff, C., Schneider, J.-L., Goff, J.R., Dominey-Howes, D., Strotz, L., 2011.
819 Expanding the proxy toolkit to help identify past events — Lessons from the
820 2004 Indian Ocean Tsunami and the 2009 South Pacific Tsunami. *Earth-Science*
821 *Reviews* 107, 107–122. doi:10.1016/j.earscirev.2011.03.007
- 822 Chagué-Goff, C., Szczuciński, W., Shinozaki, T., 2017. Applications of geochemistry
823 in tsunami research: A review. *Earth-Science Reviews* 165, 203–244.
824 doi:https://doi.org/10.1016/j.earscirev.2016.12.003
- 825 Cisternas, M., Atwater, B.F., Torrejón, F., Sawai, Y., Machuca, G., Lagos, M., Eipert,
826 A., Youlton, C., Salgado, I., Kamataki, T., Shishikura, M., Rajendran, C.P.,
827 Malik, J.K., Rizal, Y., Husni, M., 2005. Predecessors of the giant 1960 Chile
828 earthquake. *Nature* 437, 404–407. doi:10.1038/nature03943
- 829 Cisternas, M., Garrett, E., Wesson, R., Dura, T., Ely, L.L., 2017. Unusual geologic
830 evidence of coeval seismic shaking and tsunamis shows variability in earthquake
831 size and recurrence in the area of the giant 1960 Chile earthquake. *Marine*
832 *Geology* 385, 101–113. doi:10.1016/j.margeo.2016.12.007
- 833 Dura, T., Cisternas, M., Horton, B.P., Ely, L.L., Nelson, A.R., Wesson, R.L.,
834 Pilarczyk, J.E., 2015. Coastal evidence for Holocene subduction-zone
835 earthquakes and tsunamis in central Chile. *Quaternary Science Reviews* 113, 93–
836 111. doi:10.1016/j.quascirev.2014.10.015
- 837 Dura, T., Engelhart, S.E., Vacchi, M., Horton, B.P., Kopp, R.E., Peltier, W.R.,
838 Bradley, S., 2016. The Role of Holocene Relative Sea-Level Change in
839 Preserving Records of Subduction Zone Earthquakes. *Current Climate Change*
840 *Reports* 2, 86–100. doi:10.1007/s40641-016-0041-y
- 841 Ely, L.L., Cisternas, M., Wesson, R.L., Dura, T., 2014. Five centuries of tsunamis and
842 land-level changes in the overlapping rupture area of the 1960 and 2010 Chilean
843 earthquakes. *Geology* 42, 995–998. doi:10.1130/G35830.1
- 844 Fedorov, A. V, Brierley, C.M., Emanuel, K., 2010. Tropical cyclones and permanent
845 El Niño in the early Pliocene epoch. *Nature* 463, 1066–1070.
846 doi:10.1038/nature08831
- 847 Fritz, H.M., Phillips, D.A., Okayasu, A., Shimozone, T., Liu, H., Mohammed, F.,
848 Skanavis, V., Synolakis, C.E., Takahashi, T., 2012. The 2011 Japan tsunami
849 current velocity measurements from survivor videos at Kesenuma Bay using
850 LiDAR. *Geophysical Research Letters* 39, 6. doi:10.1029/2011GL050686
- 851 Garrett, E., Shennan, I., Woodroffe, S.A.A., Cisternas, M., Hocking, E.P.P., Gulliver,
852 P., 2015. Reconstructing paleoseismic deformation, 2: 1000 years of great
853 earthquakes at Chucalén, south central Chile. *Quaternary Science Reviews* 113,
854 112–122. doi:10.1016/j.quascirev.2014.10.010

- 855 Glasser, N.F., Jansson, K.N., Harrison, S., Kleman, J., 2008. The glacial
856 geomorphology and Pleistocene history of South America between 38°S and
857 56°S. *Quaternary Science Reviews* 27, 365–390.
858 doi:10.1016/j.quascirev.2007.11.011
- 859 Goto, K., Hashimoto, K., Sugawara, D., Yanagisawa, H., Abe, T., 2014. Spatial
860 thickness variability of the 2011 Tohoku-oki tsunami deposits along the coastline
861 of Sendai Bay. *Marine Geology* 358, 38–48. doi:10.1016/j.margeo.2013.12.015
- 862 Heiri, O., Lotter, A.F., Lemcke, G., 2001. Loss on ignition as a method for estimating
863 organic and carbonate content in sediments : reproducibility and comparability of
864 results. *Journal of Paleolimnology* 25, 101–110. doi:10.1023/A:1008119611481
- 865 Hogg, A.G., Hua, Q., Blackwell, P.G., Niu, M., Buck, C.E., Guilderson, T.P., Heaton,
866 T.J., Palmer, J.G., Reimer, P.J., Reimer, R.W., Turney, C.S.M., Zimmerman,
867 S.R.H., 2013. SHCal13 Southern Hemisphere Calibration, 0–50,000 Years cal
868 BP. *Radiocarbon* 55, 1889–1903. doi:10.2458/azu_js_rc.55.16783
- 869 Kelsey, H.M., Engelhart, S.E., Pilarczyk, J.E., Horton, B.P., Rubin, C.M., Daryono,
870 M.R., Ismail, N., Hawkes, A.D., Bernhardt, C.E., Cahill, N., 2015.
871 Accommodation space, relative sea level, and the archiving of paleo-earthquakes
872 along subduction zones. *Geology* 43, 675–678. doi:10.1130/G36706.1
- 873 Kelsey, H.M., Nelson, A.R., Hemphill-Haley, E., Witter, R.C., 2005. Tsunami history
874 of an Oregon coastal lake reveals a 4600 yr record of great earthquakes on the
875 Cascadia subduction zone. *Geological Society of America Bulletin* 117, 1009–
876 1032. doi:10.1130/B25452.1
- 877 Kempf, P., 2016. Tsunamis in south central Chile: evidence from coastal lakes. Ghent
878 University.
- 879 Kempf, P., Moernaut, J., Batist, M. De, 2018. Bimodal Recurrence Pattern of
880 Tsunamis in South-Central Chile: A Statistical Exploration of Paleotsunami
881 Data. *Seismological Research Letters* 90, 194–202. doi:10.1785/0220180204
- 882 Kempf, P., Moernaut, J., Van Daele, M., Vandoorne, W., Pino, M., Urrutia, R., De
883 Batist, M., 2017. Coastal lake sediments reveal 5500 years of tsunami history in
884 south central Chile. *Quaternary Science Reviews* 161, 99–116.
885 doi:http://doi.org/10.1016/j.quascirev.2017.02.018
- 886 Kempf, P., Moernaut, J., Van Daele, M., Vermassen, F., Vandoorne, W., Pino, M.,
887 Urrutia, R., Schmidt, S., Garrett, E., De Batist, M., 2015. The sedimentary record
888 of the 1960 tsunami in two coastal lakes on Isla de Chiloé, south central Chile.
889 *Sedimentary Geology* 328, 73–86. doi:10.1016/j.sedgeo.2015.08.004
- 890 Kennedy, J., 1963. The mechanics of dunes and antidunes in erodible-bed channels.
891 *Journal of Fluid Mechanics* 16, 521–544. doi:10.1017/S0022112063000975
- 892 Kortekaas, S., Dawson, A.G., 2007. Distinguishing tsunami and storm deposits: An
893 example from Martinhal, SW Portugal. *Sedimentary Geology* 200, 208–221.

- 894 doi:<https://doi.org/10.1016/j.sedgeo.2007.01.004>
- 895 Lamy, F., Kilian, R., Arz, H.W., Francois, J.-P., Kaiser, J., Prange, M., Steinke, T.,
896 2010. Holocene changes in the position and intensity of the southern westerly
897 wind belt. *Nature Geosci* 3, 695–699.
- 898 Lee, Sang Hoon, Jung, W.-Y., Bahk, J.J., Gardner, J.M., Kim, J.K., Lee, Su Hwan,
899 2013. Depositional features of co-genetic turbidite–debrite beds and possible
900 mechanisms for their formation in distal lobated bodies beyond the base-of-
901 slope, Ulleung Basin, East Sea (Japan Sea). *Marine Geology* 346, 124–140.
902 doi:[10.1016/j.margeo.2013.09.001](https://doi.org/10.1016/j.margeo.2013.09.001)
- 903 Lomnitz, C., 2004. Major Earthquakes of Chile: A Historical Survey, 1535-1960.
904 *Seismological Research Letters* 75, 368–378. doi:[10.1785/gssrl.75.3.368](https://doi.org/10.1785/gssrl.75.3.368)
- 905 Lomnitz, C., 1970. Major Earthquakes and Tsunamis in Chile during the period 1535
906 to 1955. *Geologische Rundschau* 59, 938–960.
- 907 Moernaut, J., Van Daele, M., Fontijn, K., Heirman, K., Kempf, P., Pino, M.,
908 Valdebenito, G., Urrutia, R., Strasser, M., De Batist, M., 2018. Larger
909 earthquakes recur more periodically: New insights in the megathrust earthquake
910 cycle from lacustrine turbidite records in south-central Chile. *Earth and Planetary
911 Science Letters* 481, 9–19. doi:<https://doi.org/10.1016/j.epsl.2017.10.016>
- 912 Moernaut, J., Van Daele, M., Heirman, K., Fontijn, K., Strasser, M., Pino, M.,
913 Urrutia, R., De Batist, M., 2014. Lacustrine turbidites as a tool for quantitative
914 earthquake reconstruction: New evidence for a variable rupture mode in south
915 central Chile. *Journal of Geophysical Research: Solid Earth* 119, 1607–1633.
916 doi:[10.1002/2013JB010738](https://doi.org/10.1002/2013JB010738)
- 917 Moreno, M.S., Bolte, J., Klotz, J., Melnick, D., 2009. Impact of megathrust geometry
918 on inversion of coseismic slip from geodetic data: Application to the 1960 Chile
919 earthquake. *Geophysical Research Letters* 36, L16310.
920 doi:[10.1029/2009GL039276](https://doi.org/10.1029/2009GL039276)
- 921 Nentwig, V., Bahlburg, H., Górecka, E., Huber, B., Bellanova, P., Witkowski, A.,
922 Encinas, A., 2018. Multiproxy analysis of tsunami deposits—The Tirúa example,
923 central Chile. *Geosphere* 14, 1067–1086. doi:[10.1130/GES01528.1](https://doi.org/10.1130/GES01528.1)
- 924 Nentwig, V., Tsukamoto, S., Frechen, M., Bahlburg, H., 2015. Reconstructing the
925 tsunami record in Tirúa, Central Chile beyond the historical record with quartz-
926 based SAR-OSL. *Quaternary Geochronology* 30, 299–305.
927 doi:<http://dx.doi.org/10.1016/j.quageo.2015.05.020>
- 928 Peters, R., Jaffe, B., Gelfenbaum, G., 2007. Distribution and sedimentary
929 characteristics of tsunami deposits along the Cascadia margin of western North
930 America. *Sedimentary Geology* 200, 372–386. doi:[10.1016/j.sedgeo.2007.01.015](https://doi.org/10.1016/j.sedgeo.2007.01.015)
- 931 Phantuwongraj, S., Choowong, M., Nanayama, F., Hisada, K.-I., Charusiri, P.,
932 Chutakositkanon, V., Pailoplee, S., Chabangbon, A., 2013. Coastal geomorphic

- 933 conditions and styles of storm surge washover deposits from Southern Thailand.
934 *Geomorphology* 192, 43–58. doi:10.1016/j.geomorph.2013.03.016
- 935 Plafker, G., Savage, J.C., 1970. Mechanism of the Chilean Earthquakes of May 21
936 and 22 , 1960. *Geological Society of America Bulletin* 81, 1001–1030.
937 doi:10.1130/0016-7606(1970)81
- 938 Reinhardt, E.G., Nairn, R.B., Lopez, G., 2010. Recovery estimates for the Río Cruces
939 after the May 1960 Chilean earthquake. *Marine Geology* 269, 18–33.
940 doi:10.1016/j.margeo.2009.12.003
- 941 Siddall, M., Rohling, E.J., Almogi-Labin, A., Hemleben, C., Meischner, D.,
942 Schmelzer, I., Smeed, D.A., 2003. Sea-level fluctuations during the last glacial
943 cycle. *Nature* 423, 853–858.
- 944 Sievers, H., Villegas, G.C., Barros, G., 1963. The seismic sea wave of 22 May 1960
945 along the Chilean coast. *Bulletin of the Seismological Society of America* 53,
946 1125–1190.
- 947 Stefer, S., Moernaut, J., Melnick, D., Echtler, H.P., Arz, H.W., Lamy, F., De Batist,
948 M., Oncken, O., Haug, G.H., 2010. Forearc uplift rates deduced from sediment
949 cores of two coastal lakes in south-central Chile. *Tectonophysics* 495, 129–143.
950 doi:http://dx.doi.org/10.1016/j.tecto.2009.05.006
- 951 Valdovinos, C., Pedreros, P., 2007. Geographic variations in shell growth rates of the
952 mussel *Diplodon chilensis* from temperate lakes of Chile: Implications for
953 biodiversity conservation. *Limnologica* 37, 63–75.
954 doi:https://doi.org/10.1016/j.limno.2006.08.007
- 955 Van Daele, M., Araya-Cornejo, C., Pille, T., Vanneste, K., Moernaut, J., Schmidt, S.,
956 Kempf, P., Meyer, I., Cisternas, M., 2019. Distinguishing intraplate from
957 megathrust earthquakes using lacustrine turbidites. *Geology* 47, 127–130.
- 958 Van Daele, M., Cnudde, V., Duyck, P., Pino, M., Urrutia, R., De Batist, M., 2014.
959 Multidirectional, synchronously-triggered seismo-turbidites and debrites
960 revealed by X-ray computed tomography (CT). *Sedimentology* 61, 861–880.
961 doi:10.1111/sed.12070
- 962 Villalobos, L., Parra, O., Grandjean, M., Jaque, E., Woelfl, S., Campos, H., 2003. A
963 study of the river basins and limnology of five humic lakes on Chiloé Island.
964 *Revista chilena de historia natural* 76. doi:10.4067/S0716-078X2003000400003
- 965 Wesson, R.L., Melnick, D., Cisternas, M., Moreno, M., Ely, L.L., 2015. Vertical
966 deformation through a complete seismic cycle at Isla Santa Maria, Chile. *Nature*
967 *Geoscience* 8, 547–551.
- 968